Multicell Squall-Line Structure as a Manifestation of Vertically Trapped Gravity Waves

MING-JEN YANG AND ROBERT A. HOUZE JR.

Department of Atmospheric Sciences, University of Washington, Seattle, Washington

(Manuscript received 28 February 1994, in final form 8 July 1994)

ABSTRACT

Two-dimensional and three-dimensional simulations of a midlatitude squall line with a high-resolution nonhydrostatic model suggest that the multicellular structure of the storm may be associated with gravity waves generated by convection. Time-lapse display of model output demonstrates that the commonly described "cut-off" process is actually a gravity wave phenomenon. The convective cells arise as gravity waves, which are forced by continuous strong low-level convergence at the storm's gust front. The waves propagate to both sides of the gust front. The stronger westward (front to rear) mode dominates at the mature stage of the squall line. Continuous low-level updraft is generated at the nose of the cold pool, which propagates at the speed of a density current. Updraft cells periodically break away from this persistent low-level gust-front updraft and move at phase speeds of their associated gravity waves, not at the surrounding airflow speeds as implied by the traditional multicell model.

Linear theory shows that the multicellular structure is associated with vertically trapped gravity waves in the troposphere. The waves become trapped in the mid- to upper troposphere because of the strong decrease of Scorer parameter with height as a result of strong vertical wind shear and the reduced static stability aloft. Waves are trapped in lower levels because of the rigid ground. The basic characteristics of these trapped tropospheric gravity waves are wavelengths of 16–20 km, storm-relative phase speeds of 20–25 m s^{-1}, and periods of 11–17 min, which are consistent with the generation periods of precipitation cells at the mature stage in the leading portion of the storm. In the trailing stratiform region, these tropospheric gravity waves become more diffuse with weaker amplitudes, and their wavelengths become longer (25–35 km) with greater storm-relative phase speeds (30–40 m s^{-1}), as described by the dispersion relationship of internal gravity waves.

The tropospheric gravity waves differ from disturbances above the tropopause, which are mechanically forced by convective cells impinging on the tropopause. These waves in the lower stratosphere have the structure of vertically propagating (rather than trapped) gravity waves.

1. Introduction

The fundamental building block of thunderstorms is the "cell" (Byers and Braham 1949), which is characterized by a compact region of relatively strong vertical velocity and intense precipitation. In general, there are two kinds of cells—ordinary cells and supercells—and the majority of convective storms are composed of ordinary cells (Browning 1977; Weisman and Klemp 1984). Convective storms often consist of several ordinary cells at different stages of evolution. Byers and Braham (1949) identified three stages in the evolution of an ordinary cell: the cumulus stage (updraft alone), the mature stage (updraft and downdraft), and the dissipating stage (downdraft alone). The mature stage of a typical cell lasts approximately 15–30 min before giving way to the dissipating stage.

A multicell storm often has cells forming on a preferred side, with each individual cell moving roughly parallel to the mean midtropospheric wind vector. The storm thus propagates discretely toward either the right or the left of the mean wind vector (Browning 1962; Marwitz 1972; Newton and Fankhauser 1975). A vertical cross section for a Colorado multicell hailstorm based on radar and aircraft data as synthesized by Browning et al. (1976) is shown in Fig. 1. This vertical cross section, taken along the storm's direction of motion, shows a sequence of four ordinary cells ($n - 2$, $n - 1$, n, $n + 1$) at different stages of evolution. Each cell goes through a similar life cycle, with new cells developing on the storm's forward flank (right side of figure) and old cells decaying on the rear flank (left side of figure). This schematic model can be interpreted in two ways: as an instantaneous view of a typical multicell storm with four cells at different stages of evolution, or as four stages in the evolution of an individual cell. The time interval between development of successive cells was about 15 min. The lifetime of each cell was less than 60 min.

Ordinary multicell storms are often characterized by the successive formation of "discrete" new cells; each cell is essentially independent from those previously existing (Marwitz 1972; Browning 1977; Wilhelmson and Chen 1982). However, Foote and Frank (1983) described another mode of multicell

Corresponding author address: Ming-Jen Yang, Dept. of Atmospheric Sciences, AK-40, University of Washington, Seattle, WA 98195.

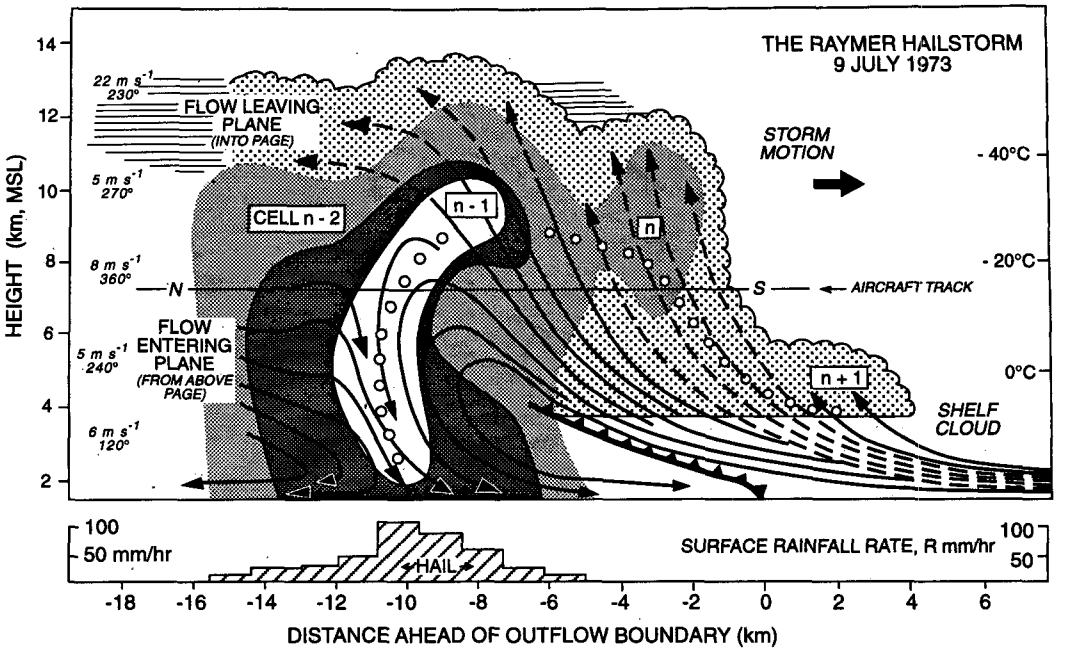

FIG. 1. Schematic model of a multicell storm in northern Colorado showing a vertical section along its direction of motion. Thick lines are smoothed streamlines of flow relative to the moving storm; they are broken on the left side of the figure to represent flow into and out of the plane and on the right side of the figure to represent flow remaining within a plane a few kilometers closer to the reader. Lightly stippled shading: extent of cloud; darker grades of shading: radar reflectivities of 35, 45, and 50 dBZ; open circles: trajectory of a hailstone during its growth from a small particle. Right: temperature scale; temperature of a parcel lifted from the surface. Left: environmental winds relative to the storm based on soundings behind the storm. Surface rainfall rates averaged over 2-min intervals during the passage of the storm are plotted at the bottom of the figure (from Browning et al. 1976).

storm based on a triple-Doppler radar analysis. The individual cells in this storm (the middle panels in Fig. 2) were neither fully independent to be considered as those in a classic multicell storm nor sufficiently steady to be considered as a supercell. Foote and Frank (1983) called this behavior "weak evolution" in contrast with the classic or "strong evolution" multicell model, because the appearance of a cell's updraft is considered to be a small perturbation on an established, persistent updraft.

A squall line is a long-lived line of convective cells. It consists of laterally aligned cells that tend not to interfere disruptively with one another by competing for the same warm, moist environmental air. Individual cells within a squall line may be all ordinary cells, a mixture of ordinary cells and supercells, or all supercells. A vertical cross section taken perpendicular to the squall line often shows a series of convective cells at different stages of their evolution as shown in Fig. 1.

Fovell and Ogura (1988, hereafter referred to as FO) investigated the multicellular structure of the 22 May 1976 Oklahoma squall line with a two-dimensional nonhydrostatic numerical model. Their simulated multicell storm reached a "quasi-equilibrium" state characterized by periodic production of new cells at the leading edge of the storm. Individual cells moved rearward relative to the gust front as they aged, transporting hydrometeors in their updrafts into the trailing portion of the storm. The multicellular behavior of the squall line was interpreted in terms of the new cells cutting off the moisture supply of the older cells.

The objective of this study is to consider the multicellular structure of a midlatitude squall line from the viewpoint of gravity wave dynamics. The squall line case to be investigated in this study is the 10–11 June 1985 squall line observed during the PRE-STORM project (Preliminary Regional Experiment for Storm-scale Operational Research Meteorology) (Cunning 1986). The 10–11 June squall line has been investigated in several observational studies (e.g., Smull and Houze 1987; Rutledge et al. 1988; Johnson and Hamilton 1988; Biggerstaff and Houze 1991a,b, 1993; Braun and Houze 1994) and numerical studies (Zhang et al. 1989; Zhang and Gao 1989). None of these studies examined the gravity wave structure excited by convection of the squall line system, which is the focus of this study. Numerical simulation results of the 10–11 June 1985 squall line with a high-resolution nonhydrostatic cloud model will be analyzed. A linear theory will be presented to explain how the multicellular structure of the squall line may be explained in terms of gravity waves generated at the gust front and trapped within the troposphere.

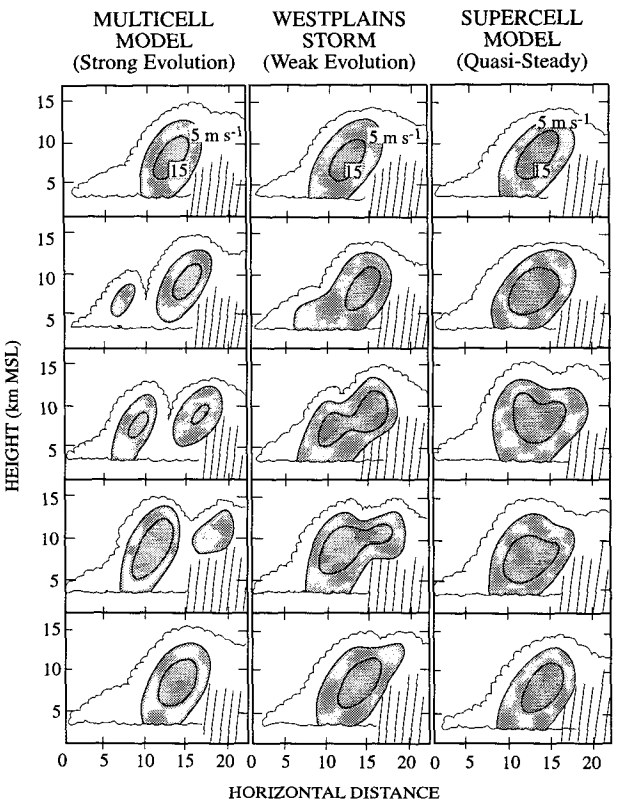

FIG. 2. Schematic diagram showing updraft evolution for three different storm models. Contours represent isotachs of vertical wind speed. Time between successive frames, moving down the figure, is 3–5 min. Vertical velocity of updraft greater than 15 m s^{-1} is heavily shaded, and vertical velocity of updraft between 5 and 15 m s^{-1} is lightly shaded (from Foote and Frank 1983).

2. Numerical model and initial conditions

a. Numerical model

The numerical model used in this study is the Klemp and Wilhelmson (1978; hereafter referred to as KW) compressible nonhydrostatic cloud model, as modified by Wilhelmson and Chen (1982). Microphysical bulk parameterization is described by Lin et al. (1983), with improvements suggested by Potter (1991). Ice-phase microphysics is included. Both two-dimensional (2D) and three-dimensional (3D) versions of the model are used. The x coordinate is the cross-line direction and the y coordinate is the along-line direction. The basic-state environment is assumed constant in time and horizontally homogeneous; large-scale variation, Coriolis force, surface drag, and radiation effects are neglected.

For the 2D simulation, the grid is stretched in both vertical (z) and cross-line (x) directions in order to optimize the grid resolution. There are 62 grid points in the vertical; the model top is at 21.7 km, and the grid size (Δz) of the lowest layer is 140 m, while the grid size of the highest layer is 550 m. A rigid lid is used at the top and bottom of the domain. The implementation of horizontally stretched grids is similar to that of FO. The model uses 455 grid points in the horizontal, the central 315 of which comprise a fine mesh with a constant grid size of 1 km. A 2250-km-wide stretch grid is put on both sides of the fine mesh; the ratio between adjacent grid spacings is 1.075:1. The total horizontal domain size (fine mesh and stretched grids) is thus 4814 km. An "open" boundary condition described by KW with phase speed $c^* = 30$ m s^{-1} is used to reduce the numerical reflection at the lateral boundaries. During the course of the simulation, the model domain translates with the storm so that the simulated storm is always within the fine mesh. A time-splitting scheme is used to provide numerical efficiency by treating the sound wave mode (2-s time step) and the gravity wave mode (6-s time step) separately (see KW for details).

b. Initial conditions

The smoothed initial temperature and dewpoint profiles for the simulation were taken from the 2331 UTC 10 June 1985 sounding of Enid (END), Oklahoma (Fig. 3a). This sounding was taken at a location in the path of the bowed part of the 10–11 June squall line (Fig. 4), which passed this station 4 h later. Extra moisture was added to the Enid sounding in the low levels in order to favor convection. Without the extra low-level moisture, the simulated storm died 2 h after its initiation. This enhanced low-level moisture profile was based on the 2330 UTC 10 June 1985 sounding of Pratt, Kansas (the PTT station in Fig. 4). The low-level moisture profile from the Pratt sounding was used because this station was more "optimally located" in the vicinity of early storm development, and its dewpoint profile is probably more representative of the moisture characteristics of the storm's initial environment. The vertical profile of the smoothed initial wind components is shown in Fig. 3b. The convective available potential energy (CAPE) (Moncrieff and Miller 1976; Weisman and Klemp 1982) calculated from this moisture-enhanced sounding is 3323 J kg^{-1}, which is higher than the average value of 2820 J kg^{-1} for springtime broken-line type squall lines in this region (Bluestein and Jain 1985). The bulk Richardson number (Weisman and Klemp 1982; Bluestein and Jain 1985) calculated from the moisture-enhanced sounding and observed wind fields (including both the cross-line and along-line components) is 46.9, which is in the range of multicell storms (Weisman and Klemp 1982). A 5-km-deep, 170-km-long cold pool of $\Delta\theta' = -6$ K and $\Delta q_v' = -4$ g kg^{-1} (in Fig. 5) was placed in the domain to initiate convection. This initial cold pool, which was prescribed as a negative potential temperature and moisture perturbation, was set to mimic the background cold air produced by a decaying cold front in the synoptic environment (Johnson and Hamilton 1988). The characteristics of the cold pool were determined from the analysis of surface mesonetwork data (see Fig. 5 of Johnson and Hamilton 1988).

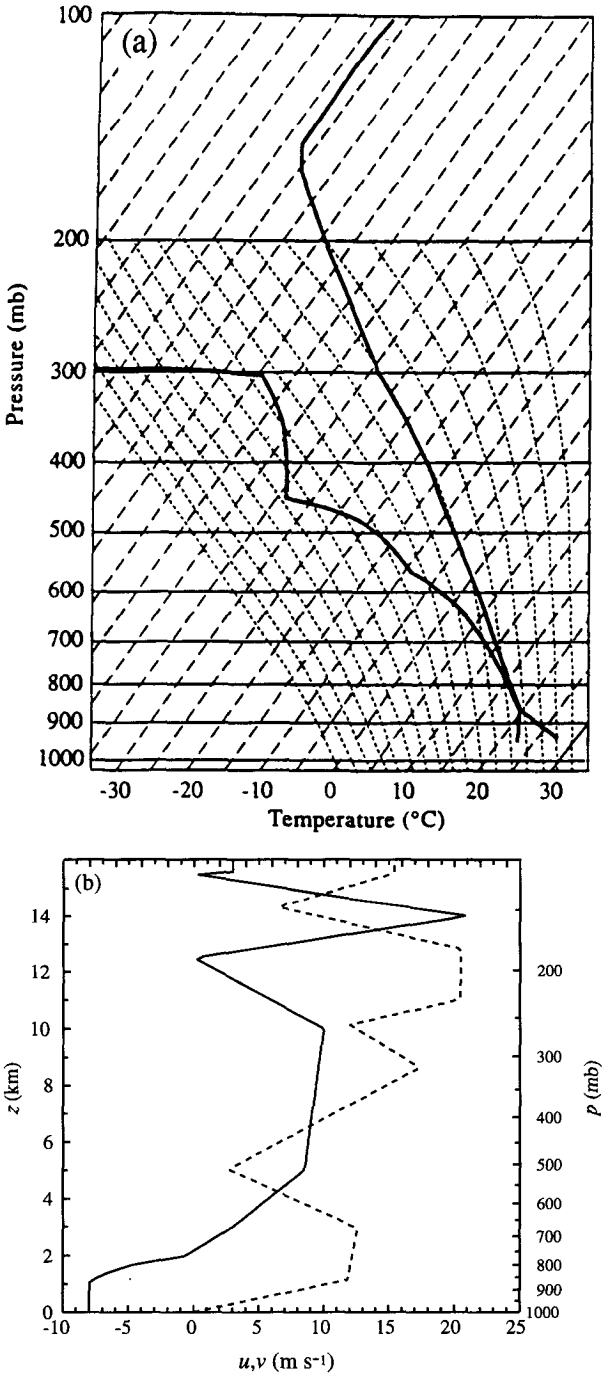

FIG. 3. (a) Temperature and dewpoint soundings displayed in a skew T–log$p$ diagram and (b) the wind components of Enid, Oklahoma, on 2331 UTC 10 June 1985. Solid line in (b) is the cross-line component of the ground-relative wind, and the dashed line is the along-line component.

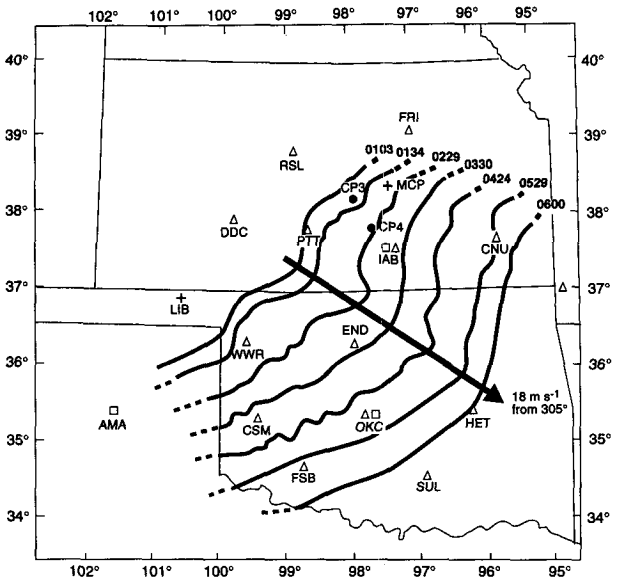

FIG. 4. Isochrones of the leading edge of the 10–11 June 1985 squall line. Dashes indicate that the true end of the squall line extends beyond that shown. The heavy, straight arrow shows the location of the squall line center as a function of time (from Biggerstaff and Houze 1991a).

3. Two-dimensional simulation results

For the simulated 2D storm, the initial cold pool generates a convective cell, which leans downshear (ahead of the moving line) with height owing to the strong ambient wind shear. The development of convection follows a pattern similar to that described by Rotunno et al. (1988). By t = 30 min, a substantial burst of rainfall reaches the ground and the anvil outflow is mostly in the downshear direction. A sequence of cells that develop along the leading edge of the cold pool

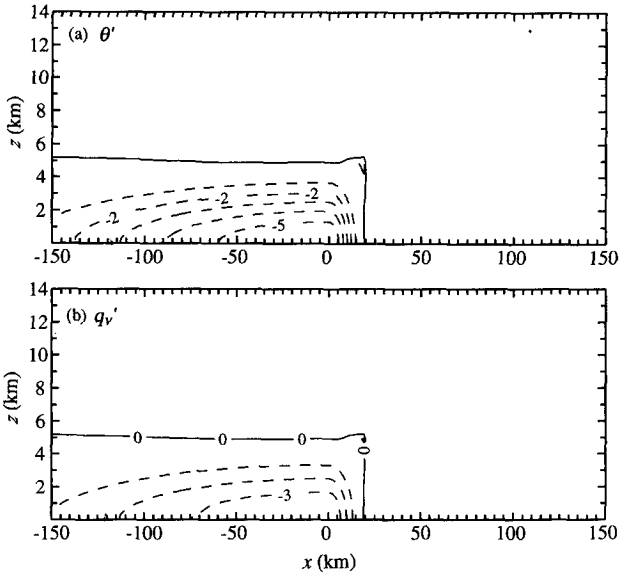

FIG. 5. (a) Potential temperature perturbation (with a contour interval of 1 K) and (b) water vapor mixing ratio perturbation (with a contour interval of 1 g kg^{-1}) of the cold pool used to initiate convection. Negative fields are dashed.

continues to lean downshear with height through 2 h. At t = 2 h the updraft cells are vertically oriented, with anvil outflows more evenly distributed in the upshear and downshear directions. After t = 2 h the simulated storm leans increasingly upshear (rearward) with height and cell redevelopment continues to occur at the leading edge as the precipitation-induced cold pool intensifies its strength. After t = 5 h the width of the surface precipitation region increases with time, and the cell production proceeds in a regular, periodic manner.

a. Mesoscale structure

After t = 8 h, the simulated 2D squall line reaches its mature stage and shows a qualitatively realistic structure when compared with observations. Figure 6a is the time sequence of surface rainfall rate during a 1-h period (t = 10–11 h) in the mature stage. It shows the continuous generation of intense precipitation cells at the leading edge and much weaker precipitation in the trailing stratiform region. Figure 6b displays the 1-h time-averaged surface rainfall rate, which shows the heavy precipitation in the convective region (from x = 20 to 50 km), followed by weak rainfall in the transition zone (from x = 0 to 20 km) and a secondary rainfall maximum in the stratiform region (from x = −90 to 0 km). This surface rainfall rate field is in good agreement with the low-level radar reflectivity field (see Fig. 6 of Biggerstaff and Houze 1991a). Note that the gust front is fixed near x = 50 km.

Figures 7 and 8 depict time-averaged model output fields in the fine mesh during the same 1-h period (t = 10–11 h) at the mature stage. Time averaging is applied to each field over this 1-h period at a 2-min data interval, similar to FO. Thus convective-scale, transient wavelike perturbations are smoothed out, and only more steady mesoscale signatures are left. All fields are displayed in a coordinate translating at the gust-front propagation speed (12 m s^{-1} during this time period).

Figure 7a is the storm-relative horizontal wind field (storm speed is determined as the gust-front propagation speed) that exhibits front-to-rear (FTR; negative) flows in mid- to upper levels within the storm (x = −90 to 50 km) and in lower levels at the back edge of the storm (x = −90 to −60 km) and rear-to-front (RTF; positive) flows in between. The RTF flow occurs at the rear of the system as a rear inflow jet, and it penetrates downward and across the storm into the convective region (x = 20 to 50 km). The time-averaged model winds of the simulated 2D storm agree well with the along-line-averaged wind field in Fig. 7b based on the dual-Doppler radar composite analysis of Biggerstaff and Houze (1993), although the simulated FTR jet is stronger than the "observed" one as a result of the exaggerated horizontal divergence by the restricted 2D geometry (Nicholls and Weissbluth 1988; Weisman 1992, personal communication). The length in the along-line direction included in the average of the observations is 60 km, which covers four to six convective cells, roughly the same number of

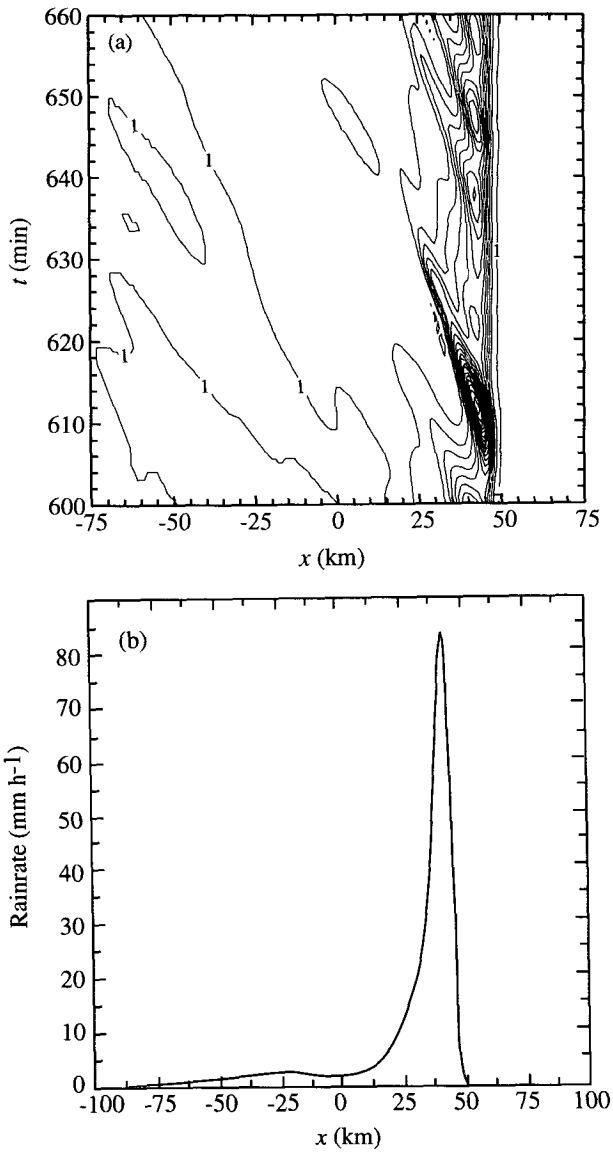

FIG. 6. (a) Time history of surface rainfall rate during a 1-h period (600–660 min) and (b) the 1-h-averaged surface rainfall rate at the mature stage of the simulated 2D storm. Contour lines in (a) start from 1 mm h^{-1}, with an interval of 10 mm h^{-1}. It is displayed in a storm-relative coordinate system moving at a speed of 12 m s^{-1} relative to the ground.

precipitation cells included in the time average (see Fig. 6a) for the simulated 2D storm.

Figure 8a is the vertical velocity field of the simulated 2D storm, which shows an intense low-level updraft maximum, another one at midlevels in the convective region (x = 20 to 50 km), and much broader but weaker mesoscale updrafts and downdrafts in the stratiform region (x = −90 to 0 km). A downdraft also occurs in the upper levels in the transition zone (x = 0 to 20 km) in Fig. 8a, although it is too weak to show

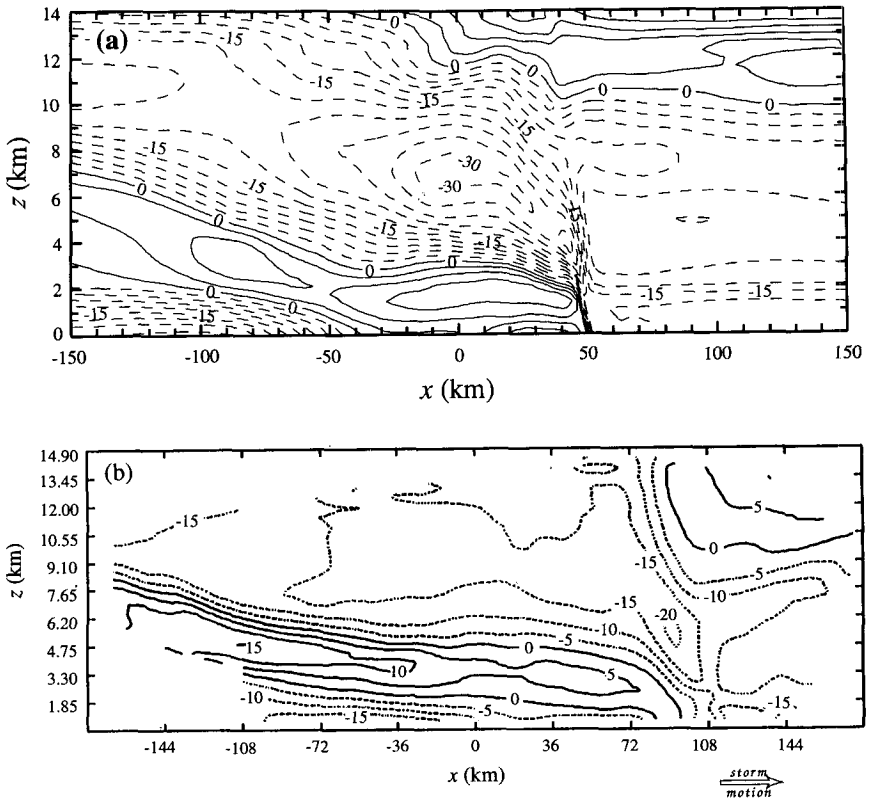

FIG. 7. (a) Time-averaged storm-relative cross-line wind field (with a contour interval of 3 m s^{-1}) of the 2D simulation and (b) the along-line-averaged cross-line wind field (with a contour interval of 5 m s^{-1}) based on the dual-Doppler radar analysis (Biggerstaff and Houze 1993). Solid lines are rear-to-front (positive) flows, and dashed lines are front-to-rear (negative) flows.

up with the 0.5 m s^{-1} contour interval. These features agree well with the along-line-averaged vertical velocity field in Fig. 8b from the dual-Doppler radar composite analysis (Biggerstaff and Houze 1993). In particular, the model successfully simulates the downward slope of mesoscale downdrafts toward the convective region. The simulation also shows that the mesoscale updrafts are ahead (to the right) of the mesoscale downdrafts in the stratiform precipitation region (x = −90 to 0 km). This structure is also consistent with the radar composite analysis (Fig. 8b). The low-level updraft maximum at the gust front does not show up well in the radar composite analysis because the divergence in the boundary layer was not sampled well by radar as a result of beam geometry, the earth's curvature, and refraction of the radar beam by the ground.

b. Transient convective structure

The realistic structure of the time-averaged simulation results (Figs. 7a and 8a), when qualitatively compared with the dual-Doppler radar composite analysis (Figs. 7b and 8b), gives us confidence to analyze the model results in more detail. The time averaging required to make the comparisons smears out convective-scale phenomenon, which cannot be resolved by the dual-Doppler radar composite analysis but can be simulated with the high-resolution cloud model. These convective-scale, transient features are evident in instantaneous model outputs at t = 11 h (Figs. 9–12). The vertical velocity with the hatched rainwater field and shaded snow field in Fig. 9 displays the typical structure of a multicell storm, that is, a sequence of convective cells at different stages of their evolution. However, when the vertical velocity field is superimposed on other fields (like pressure perturbation p' in Fig. 10, horizontal wind u in Fig. 11, or potential temperature perturbation θ' in Fig. 12), a new interpretation of the multicellular structure can be obtained—*convective cells in a multicell storm are associated with gravity waves.*

In Fig. 10, low pressure perturbations p' (defined as the deviations from the initial value; indicated by "L") are located one-quarter of a wavelength behind (to the left of) the updrafts (indicated by the heavy shading) at low levels (z < 3.5 km), but the minima p' are located one-quarter of a wavelength ahead (to the right) of the updrafts in upper levels (7 km < z < 13 km). This phase relationship can be seen clearly for the updraft located at x = 13 to 23 km. Although the

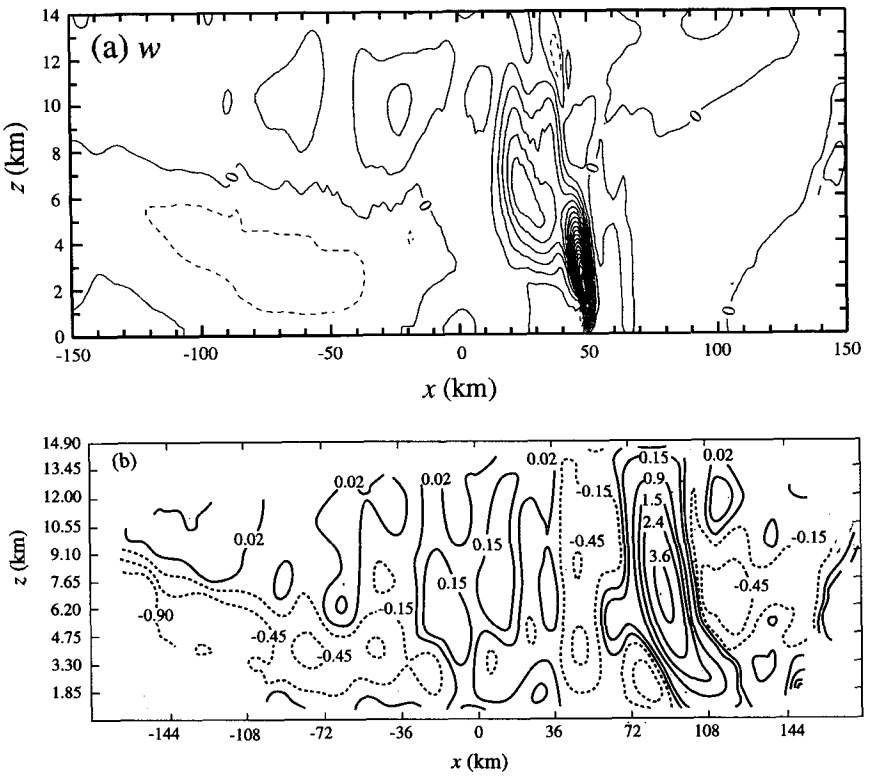

FIG. 8. (a) Time-averaged vertical velocity field (with a contour interval of 0.5 m s^{-1}) of the 2D simulation and (b) the vertical velocity field based on the dual-Doppler radar analysis (Biggerstaff and Houze 1993). Vertical velocity in (b) is contoured at 3.6, 2.4, 1.5, 0.9, 0.15, 0.02, −0.15, −0.45, and −0.9 m s^{-1}. The positive field is in solid lines and the negative field is dashed.

heights of updraft centers for these convective cells (in Fig. 9) are different, their phase relationships with p' fields (Fig. 10) are the same. Above the tropopause ($z > 14$ km), however, low pressure perturbations are collocated with the downdrafts (indicated by the light shading). The 90° phase shift between the p' and w fields in the lower troposphere creates a strong front-to-rear pressure gradient that forces air parcels near the gust front to move rearward (see the low pressure p' centered at $z = 2.5$ km, $x = 45$ km). Similarly in Fig. 11, the horizontal wind maxima u (indicated by "M") are seen to be one-quarter of a wavelength behind (to the left of) the updrafts in low levels ($z < 3$ km), but u maxima are one-quarter of a wavelength ahead (to the right) of updrafts in upper levels (7 km $< z <$ 13 km). The updraft located at $x = 13$ to 23 km again shows the phase relationships between the w and u fields very clearly. The u maxima are collocated with the downdrafts above the tropopause ($z > 14$ km). In Fig. 12, the maximum potential temperature perturbations θ' (defined as the deviation from the initial value; indicated by "W") are one-quarter of a wavelength behind (to the left of) the updrafts in all levels, and this phase shift is more pronounced above the tropopause. The distinct phase relationships among the w, p', u, and θ' fields indicate that the multicellular structure is possibly a gravity wave phenomenon.

A similar phase relationship between w and u fields can also be found in the analysis of "nearly instantaneous" Doppler-derived wind fields for the 10–11 June 1985 squall line in Fig. 13. Figure 13a covers the rear part of the convective region and the trailing stratiform region with a clear "bright band" in the radar reflectivity field. Figure 13b shows that low-level horizontal wind maxima at $x = 12$ km and $x = 48$ km are located with updrafts to the right and downdrafts to the left (Fig. 13c), which is similar to the low-level configuration between simulated w and u fields displayed in Fig. 11.

Disturbances above the tropopause ($z > 14$ km) in Figs. 10–12 show a typical structure of vertically propagating gravity waves (cf. Fig. 4.1 of Durran 1990 or Fig. 6.6 of Gill 1982). For the rearward-moving mode (behind the gust front; $x < 50$ km), w is in phase with p', out of phase with u', and 90° ahead of θ' (w maximum is ahead of θ' maximum by one-quarter of a wavelength). For the forward-moving mode (ahead of the gust front; $x > 50$ km), w is in phase with both u' and p' and 90° behind θ' (w maximum is rearward of θ' maximum by one-quarter

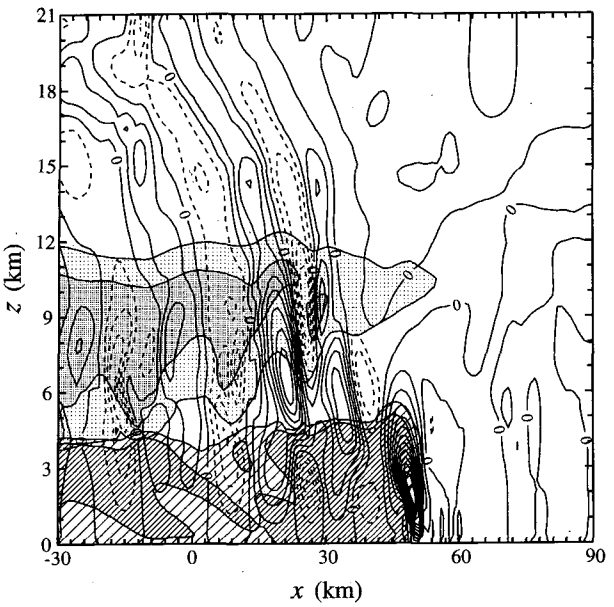

FIG. 9. Vertical velocity (with a contour interval of 1 m s^{-1}) of the simulated 2D storm at t = 11 h. The positive field is in solid lines and the negative field is dashed. Snow mixing ratio greater than 2 g kg^{-1} is lightly shaded, and snow mixing ratio greater than 4 g kg^{-1} is heavily shaded. Rainwater mixing ratio greater than 0.1 g kg^{-1} is lightly hatched, and rainwater mixing ratio greater than 0.3 g kg^{-1} is heavily hatched. The gust front is near x = 50 km.

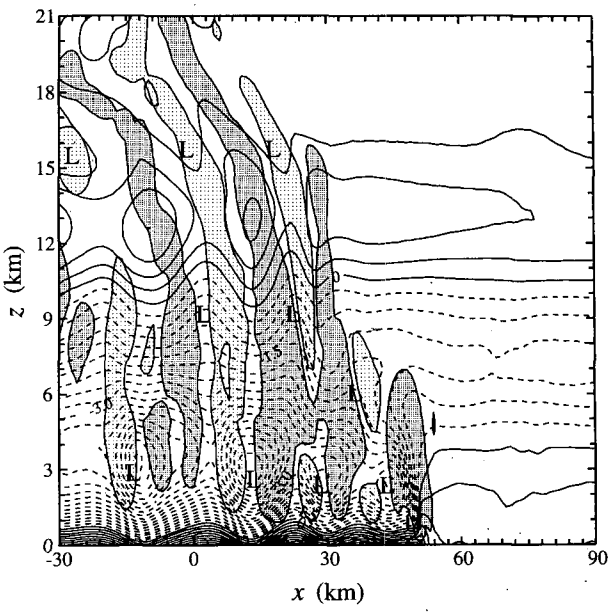

FIG. 10. Pressure perturbation (with a contour interval of 0.3 mb) of the simulated 2D storm at t = 11 h. The positive field is in solid lines and the negative field is dashed. Vertical velocity of updraft greater than 1 m s^{-1} is heavily shaded, and vertical velocity of downdraft less than −1 m s^{-1} is lightly shaded. A letter L denotes a region of low pressure. The detailed vertical velocity structure can be seen in Fig. 9.

of a wavelength), although their amplitudes are too weak to show up for the contour intervals used in Figs. 10–12. The gravity waves above the tropopause are mechanically triggered by convective cells constantly impinging upon the tropopause (Fovell et al. 1992).

c. *Gravity wave interpretation*

Figure 14 is a time sequence of the vertical velocity field of the 2D simulation, which shows that the low-level convective updraft at the gust front (x = 50 km) is a persistent feature of the simulated mature-phase squall line. The occurrence of a persistent low-level updraft at the gust front is also found by Fovell and Ogura (1989) in their simulated Oklahoma multicell storm. Convective cells behind the low-level gust-front cell, on the other hand, are transient wave features. A new "gravity wave" updraft G_1 first occurs near x = 40 km at t = 644 min. It forms by breaking away from the top of the low-level gust-front updraft because of the strong front-to-rear pressure gradient associated with the 90° phase shift between the p' and w fields in low levels (x = 45 km in Fig. 10). Once the convective cell is separated from the persistent gust-front updraft, it propagates rearward at its associated gravity wave phase speed (to be shown in Figs. 15–16). The next gravity wave updraft G_2 appears at the same location (x = 40 km) at t = 656 min and the cycle repeats. The fact that the location of a new convective cell relative to the gust front is the same as for the old convective cell is also documented by Sanders and Emanuel (1977) for an Oklahoma squall line and by FO for their simulated multicell storm. The period for the regener-

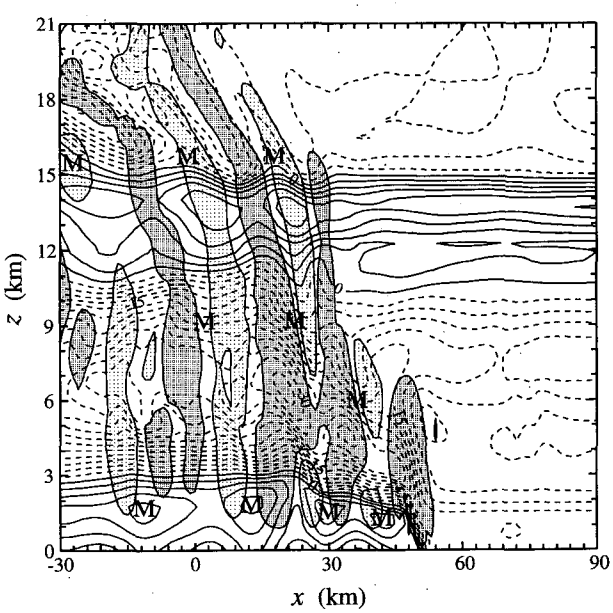

FIG. 11. As in Fig. 10 except for storm-relative horizontal wind (contour interval is 3 m s^{-1}). A letter M denotes a region of horizontal wind maximum.

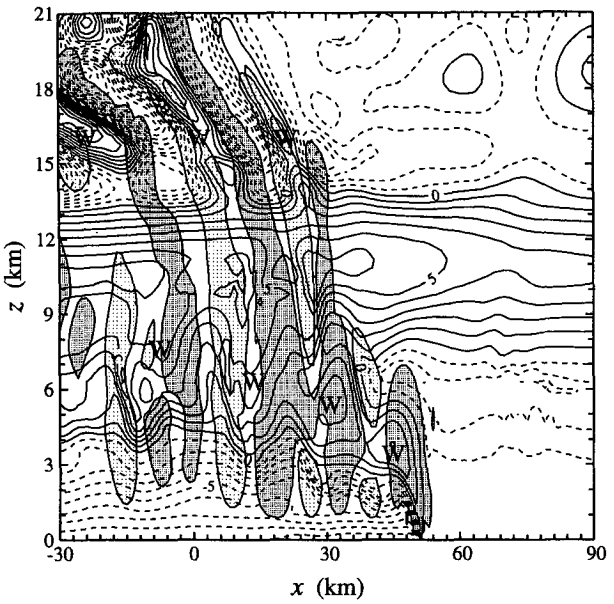

FIG. 12. As in Fig. 10 except for potential temperature perturbation (contour interval is 1 K). A letter W denotes a region of warm air.

ation of gravity wave updrafts is 12–14 min, which is the same as the generation period of precipitation cells in the surface rainfall rate field (Fig. 6a).

This behavior of the simulated multicell squall line provides a new dynamical interpretation of the multicellular structure of thunderstorms and squall lines. The traditional multicell model would suggest that the spreading cold outflow of an old cell enhances convergence, which then triggers the formation of a new cell. Once a new cell forms at the leading edge of the gust front, the supply of moisture and warm air to the older cell is cut off, causing it to dissipate (Wilhelmson and Chen 1982; Droegemeier and Wilhelmson 1985; FO). New cells thus form at the leading edge of the gust front in a "discrete" manner, according to this classic view of multicell storms (Chalon et al. 1976; Browning 1977). However, the time sequence of vertical velocity in Fig. 14 demonstrates that the gust-front updraft is a persistent feature, not a discrete or pulsating feature as implied by the classic multicell model; convective cells behind the gust front form by regularly breaking away from the top of a steady low-level gust-front updraft. The persistence or quasi steadiness of the gust-front updraft cell fits the "weak evolution" characterization of a multicell storm by Foote and Frank (1983), in which convective cells were small perturbations upon a persistent, established updraft, although the Foote and Frank mode is a highly three-dimensional entity.

The animation of model outputs thus shows that *the so-called "cutoff" process is actually a gravity wave phenomenon that has not been shown before.* The gust front and its associated low-level convergence produce a nearly steady low-level, very intense updraft. As this updraft moves through the ambient flow, it generates gravity waves. The updrafts of the gravity waves have a different propagation velocity than the gust-front updraft. A gravity wave updraft therefore periodically breaks off from the top of the gust-front updraft and moves rearward through the storm as a discrete "cell." The cutoff process associated with the multicellular storm is thus seen to be not a discrete mechanism described by the traditional multicell model but rather a continuous process of wave generation by the persistent gust front.

The convective-cell trajectories in Fig. 15a are determined by tracking the motion of updraft centers from model output at 2-min intervals during the 1-h period between t = 10 and 11 h. The convective cells are identified when their associated updrafts have a closed vertical-velocity contour during this 1-h period. Cells 1–6 in Fig. 15a do not begin and end at the same time.

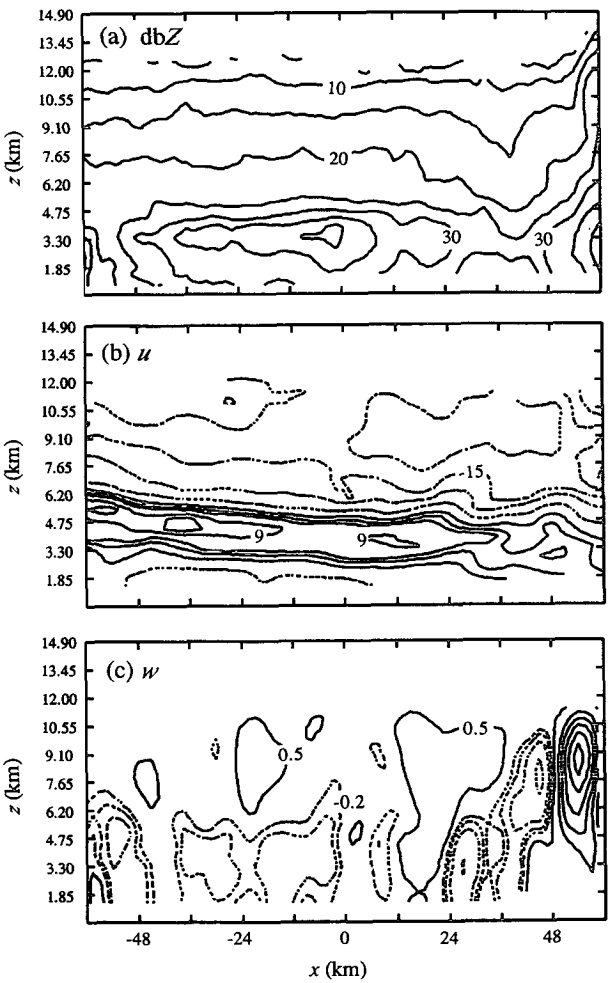

FIG. 13. (a) Dual-Doppler radar analysis showing radar reflectivity (dBZ), (b) storm-relative horizontal wind, and (c) vertical velocity at 0345 UTC 11 June 1985. Contours of reflectivity field in (a) start from 5 dBZ with a contour interval of 5 dBZ; storm-relative horizontal wind field in (b) is contoured at −21, −18, −15, −12, −6, 0, 3, 5, 9, and 12 m s^{-1}; vertical velocity field in (c) is contoured at −2, −1, −0.5, −0.2, 0.5, 2, 3, 4, 5, and 6 m s^{-1}. The positive field is in solid lines and the negative field is dashed.

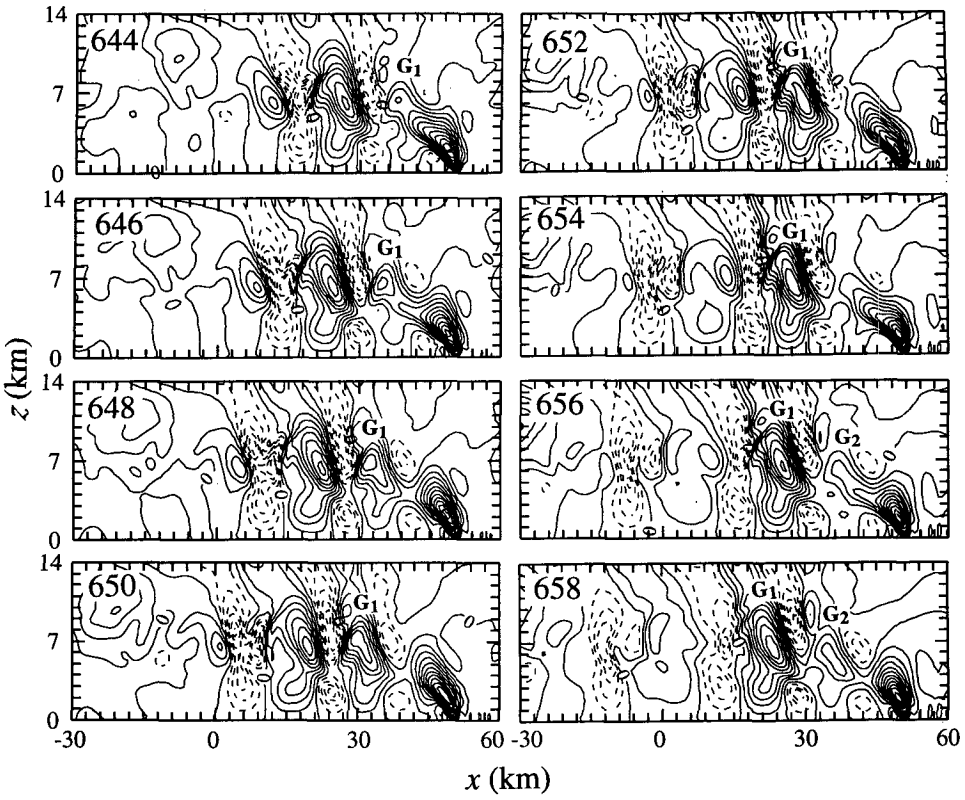

FIG. 14. Instantaneous vertical velocity contoured every 1 m s^{-1}, with negative values dashed for the 2D simulated storm. Panels are at 2-min intervals starting at t = 644 min. Gravity wave updrafts are denoted by G_1 and G_2.

The corresponding air parcel trajectories in Fig. 15b, starting from the same points as the convective updraft center trajectories in Fig. 15a, are computed by the method of Doty and Perkey (1993) from model wind fields at the same data resolution (2 min). The air parcel trajectories in Fig. 15b begin and end at the same time as the convective cell trajectories in Fig. 15a. All trajectories are displayed with respect to a storm-relative coordinate where the gust front is fixed at x = 50 km. The equivalent potential temperatures θ_e along the air parcel trajectories are found to be conserved except in the highly transient convective region (x = 20–50 km); the maximum difference of θ_e along the trajectories is less than 2 K in the strong time-variant convective region. Thus, the air-parcel trajectory calculations are believed to be computed to a satisfactory degree of accuracy.

Comparison of the convective updraft trajectories and their corresponding air-parcel trajectories shows that *the updraft cells move at velocities significantly different from the airflow in their near surroundings.* In the precipitation region (x < 50 km in Fig. 15) of the simulated mature-phase squall line, the convective updraft cells always propagate rearward relative to the gust front, regardless of the direction of the airflow in

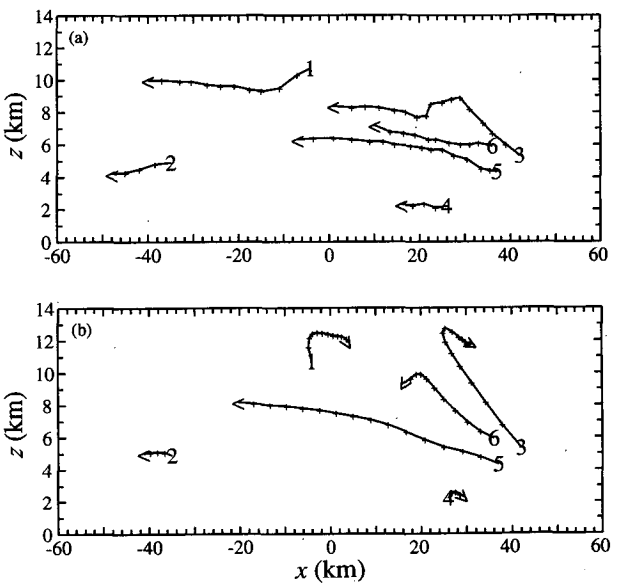

FIG. 15. (a) Convective cell (defined by the updraft center) trajectories and (b) the air-parcel trajectories starting from the same beginning points as the convective cell trajectories in (a) during the time period t = 10–11 h. Each cross (+) along the trajectories represents the position of an updraft center or an air parcel every 2 min. The arrowhead at the endpoint of each trajectory indicates its direction.

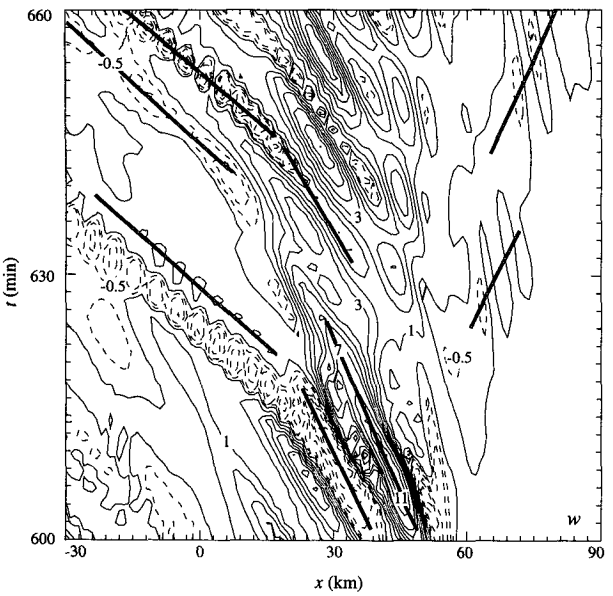

FIG. 16. Time–space plot of vertical velocity of the simulated 2D storm at $z = 5.25$ km for the time period $t = 10$–11 h. Vertical velocity is contoured at −6, −4, −3, −2, −1, −0.5, 0, 1, 2, 3, 4, 5, 6, 7, 9, and 11 m s^{-1}. The positive field is in solid lines and the negative field is dashed. Heavy solid lines are some representative constant phase lines.

their near environments. For example, convective cell trajectory 4 in Fig. 15a moves rearward (to the left of figure). However, the corresponding air parcel trajectory 4, starting from the same point in Fig. 15b, moves forward (to the right of figure) as part of the RTF airflow (see Figs. 7a and 11). Similarly, convective cell trajectories 1 and 3 in Fig. 15a move rearward, but their corresponding air-parcel trajectories 1 and 3 in Fig. 15b change to move forward at later times. Although the air-parcel trajectories all start from the same points as the convective cell trajectories, none of them end at the same point. Therefore, updraft cells that break away from the top of the low-level gust-front updraft do not move at mean airflow speeds as implied by the traditional multicell model (Browning 1977; Weisman and Klemp 1986).

Figure 16 shows the x–t plot of the w field at a height $z = 5.25$ km for the time period $t = 10$–11 h. This time–space plot of the vertical velocity field shows that the convective updraft cells are associated with gravity waves, which are initially forced at the leading edge of the storm ($x = 50$ km), and then propagate toward both sides of the leading edge with a much stronger front-to-rear mode. The dominant front-to-rear propagation of gravity waves is the result of the persistent upshear tilt of leading-edge updrafts at the mature stage (Fovell et al. 1992), when the cold pool intensifies and baroclinic vorticity generation at the leading edge of the cold pool dominates over the ambient horizontal vorticity in the low-level wind shear (Rotunno et al. 1988). The phase speeds of these gravity waves can be determined by the slopes of the constant phase lines (lines connecting w maxima and w minima) in Fig. 16. The steep slopes of the constant phase lines in the convective region ($x = 20$ to 50 km) imply slower phase speeds (storm-relative phase speeds are $c = -20$ to -25 m s^{-1}), and the flatter slopes of the constant phase lines in the stratiform region ($x < 20$ km) indicate faster phase speeds (storm-relative phase speeds are $c = -30$ to -40 m s^{-1}), as shown by the updraft cell trajectories in Fig. 15a (like trajectories 5, 6). Chalon et al. (1976), in their analysis of observed radar echoes for a Colorado multicell hailstorm, also found that convective cells moved slowly in their early stages and moved faster at their later stages. Therefore, it is clear from Figs. 15a and 16 that updraft cells move rearward with respect to the gust front at their associated gravity wave phase speeds, not at surrounding airflow speeds.

Figure 17 is the z–t plot of the w field at $x = 18$ km (32 km behind the gust front) during the same time period. This height–time plot clearly shows that above the tropopause ($z > 14$ km), constant phase lines tilt horizontally, which is a property of a vertically propagating gravity wave; below the tropopause ($z < 14$ km), constant phase lines are oriented vertically with no obvious horizontal tilt, which is a characteristic of evanescent or trapped waves. Thus the reversed quadrature relationship (90° phase shift) of the w and p' (or u) fields between the lower and upper troposphere (see Figs. 10 and 11) indicates a gravity wave structure different from those above the tropopause—*vertically trapped gravity waves.*

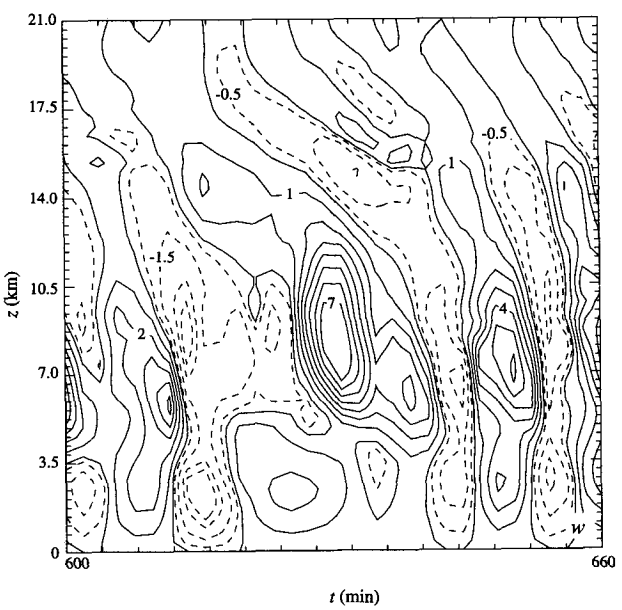

FIG. 17. Height–time plot of vertical velocity of the simulated 2D storm at $x = 18$ km for the time period $t = 10$–11 h. Vertical velocity is contoured at −6, −4, −3, −1.5, −0.5, 0, 1, 2, 3, 4, 5, 6, 7, and 9 m s^{-1}. The positive field is in solid lines and the negative field is dashed.

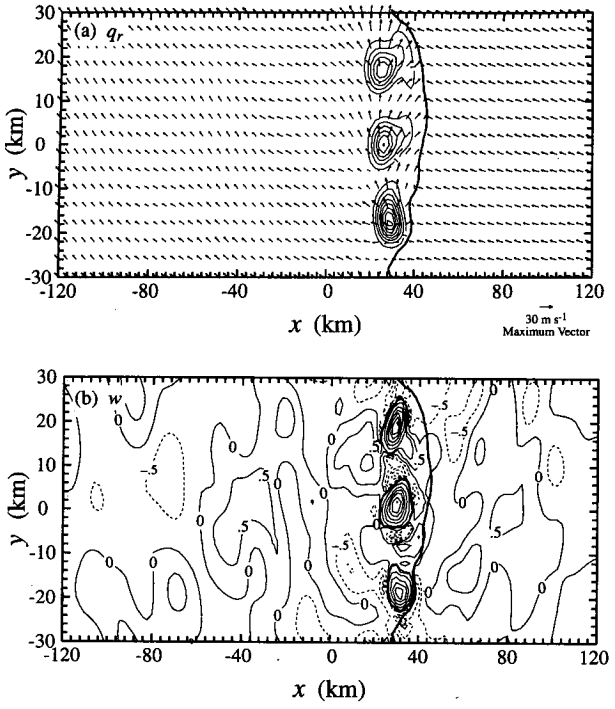

FIG. 18. (a) Surface rainwater mixing ratio and storm-relative wind vector and (b) vertical velocity at $z = 6.3$ km at $t = 5$ h for the simulated 3D storm. Contours of rainwater in (a) start at 1 g kg^{-1} with a contour interval of 1 g kg^{-1}. Wind vectors in (a) are plotted at every other grid point (4 km in x and y directions) and are drawn relative to a storm propagation speed of 7.22 m s^{-1}. A distance of two grid points (4 km) represents a vector magnitude of 30 m s^{-1}. Vertical velocity in (b) is contoured at -2, -1.5, -1, -0.5, 0, 0.5, 1, 3, 7, 11, 15, 19, and 23 m s^{-1}; the positive field is in solid lines and the negative field is dashed. The heavy line is the surface gust front determined by the $\theta' = -1$ K contour.

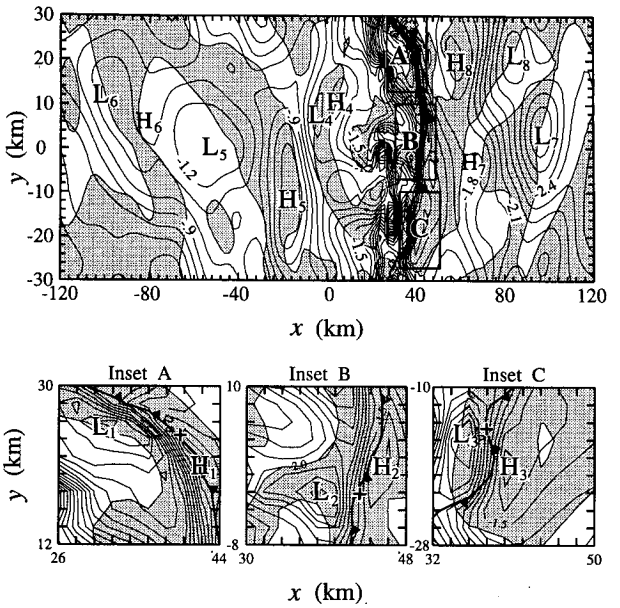

FIG. 19. Pressure perturbation p' at $z = 0.7$ km (with a contour interval of 0.1 mb), $t = 5$ h for the simulated 3D storm. The negative field is in solid lines and the areas of updrafts are shaded. The solid barbed line is the surface gust front determined by the $\theta' = -1$ K contour line. Letters H or L denote regions of high and low pressures. Insets A, B, and C highlight the w/p' phase relationships for regions with the size of 18 km × 18 km surrounding three strong convective cells near the gust front. Updraft center in each inset is indicated by a cross.

4. Three-dimensional simulation results

A 3D simulation was conducted to confirm the multicellular structure and gravity wave phenomenon found in the 2D simulation. The domain size of the 3D simulation is 240 km × 60 km × 21.7 km in x, y, and z directions, respectively. The horizontal grid size is constant ($\Delta x = \Delta y = 2$ km) and vertical grids are stretched with finer resolution at low levels (31 points in the vertical; smallest $\Delta z = 199$ m, largest $\Delta z = 1201$ m). The coarse resolution in the 3D simulation, when compared with that of the 2D simulation ($\Delta x = 1$ km; smallest $\Delta z = 140$ m, largest $\Delta z = 550$ m), is due to the constraint of computer memory and CPU. An open boundary condition is used in the cross-line (x) direction, and a periodic condition is used in the along-line (y) direction. Convection is also initiated by a cold pool as shown in Fig. 5, with a maximum strength of $\Delta\theta' = -10$ K and $\Delta q_v' = -6$ g kg^{-1} (the stronger cold pool is required for the coarser resolution in the 3D simulation). Small (<0.5 K) random temperature perturbations were superimposed on the initial line cold pool. Ice-phase microphysics is included. All other conditions are the same as in the 2D case.

The 3D counterpart to the 2D storm develops in much the same way, except that with the extra degree of freedom, the storm evolves quickly into a line of 3D cells. Figures 18–20 show the 3D simulation result at $t = 5$ h, when the simulated squall line is in its developing stage. In Fig. 18a, the rainwater mixing ratio is contoured and shown with the storm-relative wind vector field (storm motion is again determined from the gust-front propagation speed, 7.22 m s^{-1} at $t = 5$ h). Three precipitation cells are associated with three strong convective updraft cells, each accompanied by weak downdrafts (in Fig. 18b). Some weak updrafts and downdrafts (magnitudes less than 1 m s^{-1}) occurred both behind and ahead of the gust front, as in the 2D case (Fig. 9).

Figure 19 shows the w and p' fields at a low level ($z = 0.7$ km), while Fig. 20 shows the corresponding fields at an upper level ($z = 11.9$ km). At the low level (Fig. 19), three high–low couplets (H_1–L_1, H_2–L_2, and H_3–L_3) shown in insets A, B, and C are associated with three strong convective updraft cells (Fig. 18b) or three precipitation cells (Fig. 18a) just behind the gust front. High pressures are ahead of the updrafts, with low pressures behind the updrafts. A similar phase relationship can be seen for other high–low couplets (H_4–L_4, H_5–L_5, and H_6–L_6) behind the gust front. The reverse quadrature relationship (high pressures are behind updrafts with low pressures ahead of updrafts)

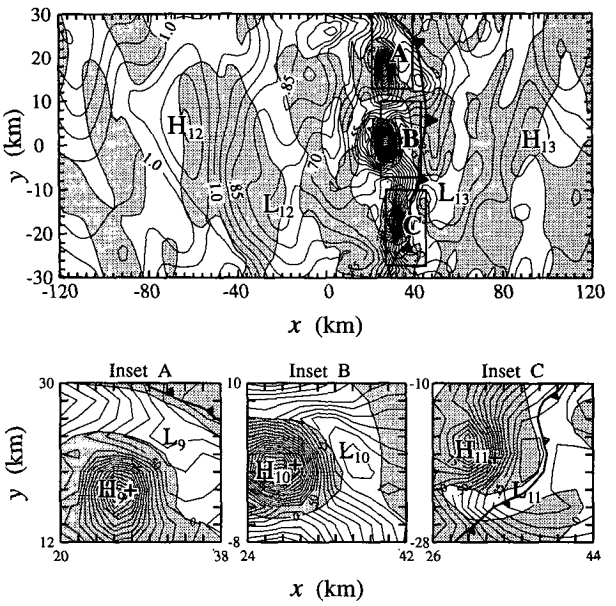

FIG. 20. As in Fig. 19 except for $z = 11.9$ km level (with a contour interval of 0.05 mb). The positive field is in solid lines.

occurs in relation to updrafts ahead of the gust front (see H_7–L_7 and H_8–L_8). These low-level phase relationships are the same as those shown in the 2D simulation (Fig. 10). At the upper level (Fig. 20), the quadrature relationships between w and p' fields are opposite to those at the low level (Fig. 19), which is again the property of vertically trapped gravity waves (see Fig. 10). In Fig. 20, high pressures (like H_9, H_{10}, H_{11}, and H_{12}) are behind the updrafts, and low pressures (like L_9, L_{10}, L_{11}, and L_{12}) are ahead of the updrafts for updrafts behind the gust front; the reverse quadrature (see H_{13}–L_{13}) again occurs to updrafts ahead of the gust front.

The quadrature relationship between w and u fields in the 3D simulation (not shown) is also similar to that seen in the 2D simulation. Therefore, we conclude that although different in details, there is no *essential* difference between the 2D and 3D simulations of the 10–11 June squall line for the multicellular structure and gravity wave phenomenon.

5. Linear theory presentation of model gravity waves

In this section, we use linear gravity wave theory to explain the multicellular structure seen in the nonlinear numerical simulation. Since the 3D results in section 4 show that the gravity wave signatures are well represented in the 2D framework, the linear theory is also 2D in order to simplify the discussion. Following Bretherton (1966), the inviscid linear governing equations for a 2D internal gravity wave in a nonrotating flow in which a basic state only varies with height are

$$\left(\frac{\partial}{\partial t} + \bar{U}\frac{\partial}{\partial x}\right)u' + w'\frac{d\bar{U}}{dz} = -c_p\bar{\theta}\frac{\partial \pi'}{\partial x} \quad (1)$$

$$\left(\frac{\partial}{\partial t} + \bar{U}\frac{\partial}{\partial x}\right)w' = -c_p\bar{\theta}\frac{\partial \pi'}{\partial z} + g\frac{\theta'}{\bar{\theta}} \quad (2)$$

$$\left(\frac{\partial}{\partial t} + \bar{U}\frac{\partial}{\partial x}\right)\theta' + \frac{\bar{\theta}}{g}N^2 w' = Q \quad (3)$$

$$\frac{c_v}{R\bar{\pi}}\left(\frac{\partial}{\partial t} + \bar{U}\frac{\partial}{\partial x}\right)\pi' + \left(\frac{\partial u'}{\partial x} + \frac{\partial w'}{\partial z}\right) - \frac{g}{c_s^2}w' = 0, \quad (4)$$

where

$$N^2 = \frac{g}{\bar{\theta}}\frac{d\bar{\theta}}{dz}, \quad c_s^2 = \frac{c_p}{c_v}R_d\bar{T} = \gamma R_d\bar{T}, \quad \pi = \left(\frac{p}{p_0}\right)^{R_d/c_p}. \quad (5)$$

Dependent variables in (1)–(4) are zonal wind u, vertical velocity w, nondimensional pressure π, and potential temperature θ, where t is time, x is the east–west coordinate, z is height, g is the magnitude of gravitational acceleration, N is the Brunt–Väisälä (buoyancy) frequency, c_p is the specific heat at constant pressure, c_v is the specific heat at constant volume, R_d is the gas constant for dry air, T is temperature, p_0 is a constant reference pressure (1000 mb), and Q is the latent heating produced by convection. The basic-state variables $\bar{\rho}$, $\bar{\theta}$, $\bar{U}$, and $\bar{\pi}$ are functions of height (z); perturbations are denoted by primes; $u = \bar{U} + u'$, $w = w'$, $\pi = \bar{\pi} + \pi'$, $\theta = \bar{\theta} + \theta'$, and c_s is the basic-state sound speed.

In order to simplify the algebra, it is useful to remove the effect of the decrease in density with height by defining new variables (Bretherton 1966):

$$\tilde{u} = \left(\frac{\bar{\rho}}{\rho_0}\right)^{1/2}u', \quad \tilde{w} = \left(\frac{\bar{\rho}}{\rho_0}\right)^{1/2}w',$$

$$\tilde{\pi} = \left(\frac{\bar{\rho}}{\rho_0}\right)^{1/2}c_p\bar{\theta}\pi', \quad \tilde{\theta} = \left(\frac{\bar{\rho}}{\rho_0}\right)^{1/2}\frac{g}{\bar{\theta}}\theta',$$

$$\tilde{Q} = \left(\frac{\bar{\rho}}{\rho_0}\right)^{1/2}\frac{g}{\bar{\theta}}Q, \quad (6)$$

where ρ_0 is a constant reference density (surface density). In terms of these new variables, the governing equations become

$$\left(\frac{\partial}{\partial t} + \bar{U}\frac{\partial}{\partial x}\right)\tilde{u} + \tilde{w}\frac{d\bar{U}}{dz} = -\frac{\partial \tilde{\pi}}{\partial x} \quad (7)$$

$$\left(\frac{\partial}{\partial t} + \bar{U}\frac{\partial}{\partial x}\right)\tilde{w} = -\frac{\partial \tilde{\pi}}{\partial z} + \tilde{\theta} - \Gamma\tilde{\pi} \quad (8)$$

$$\left(\frac{\partial}{\partial t} + \bar{U}\frac{\partial}{\partial x}\right)\tilde{\theta} + N^2\tilde{w} = \tilde{Q} \quad (9)$$

$$\frac{1}{c_s^2}\left(\frac{\partial}{\partial t}+\bar{U}\frac{\partial}{\partial x}\right)\tilde{\pi}+\frac{\partial \tilde{u}}{\partial x}+\frac{\partial \tilde{w}}{\partial z}-\Gamma\tilde{w}=0, \quad (10)$$

where

$$\Gamma=-\frac{1}{2\bar{\rho}}\frac{d\bar{\rho}}{dz}-\frac{1}{\bar{\theta}}\frac{d\bar{\theta}}{dz}=\frac{1}{2\bar{\rho}}\frac{d\bar{\rho}}{dz}+\frac{g}{c_s^2}. \quad (11)$$

Consider the case of an anelastic system only, that is, $c_s \to \infty$. Then the continuity equation (10) can be written in a simpler form,

$$\frac{\partial \tilde{u}}{\partial x}+\frac{\partial \tilde{w}}{\partial z}-\Gamma\tilde{w}=0. \quad (12)$$

Note that under the anelastic approximation (Wilhelmson and Ogura 1972), $\Gamma \approx -(2\bar{\rho})^{-1}d\bar{\rho}/dz$, and the continuity equation (12) can be rewritten in the traditional form for the anelastic continuity equation,

$$\frac{\partial}{\partial x}(\bar{\rho}u')+\frac{\partial}{\partial z}(\bar{\rho}w')=0.$$

After some algebraic manipulation of (7)–(9) with the aid of (12) (see the appendix for a detailed derivation), we obtain a single equation for $\tilde{w}$,

$$\left(\frac{\partial}{\partial t}+\bar{U}\frac{\partial}{\partial x}\right)^2\left(\frac{\partial^2\tilde{w}}{\partial x^2}+\frac{\partial^2\tilde{w}}{\partial z^2}\right)$$
$$-\frac{d^2\bar{U}}{dz^2}\left(\frac{\partial}{\partial t}+\bar{U}\frac{\partial}{\partial x}\right)\frac{\partial\tilde{w}}{\partial x}$$
$$-\left(\Gamma^2+\frac{d\Gamma}{dz}\right)\left(\frac{\partial}{\partial t}+\bar{U}\frac{\partial}{\partial x}\right)^2\tilde{w}$$
$$-2\Gamma\frac{d\bar{U}}{dz}\left(\frac{\partial}{\partial t}+\bar{U}\frac{\partial}{\partial x}\right)\frac{\partial\tilde{w}}{\partial x}$$
$$+N^2\frac{\partial^2\tilde{w}}{\partial x^2}-\frac{\partial^2\tilde{Q}}{\partial x^2}=0. \quad (13)$$

Note that some simplified versions of (13) have been used for the discussion of internal gravity waves (Scorer 1949; Sawyer 1960; Bretherton 1966; Durran 1990). Since $\bar{U}$, N^2, and Γ are functions of height, we can assume solutions for (13) of the form

$$\tilde{w}=\mathrm{Re}[W(z)e^{ik(x-ct)}],$$
$$\tilde{Q}=\mathrm{Re}[H(z)e^{ik(x-ct)}], \quad (14)$$

where Re means the real part of a complex variable, k is the wavenumber, and c is the phase speed. In (14), we assume that latent heating $\tilde{Q}$ is horizontally in phase with $\tilde{w}$, which is generally true for deep convection. Substitution of (14) into (13) leads to the so-called Taylor–Goldstein equation (with the inclusion of heating), which determines the vertical structure of W,

$$\frac{d^2W}{dz^2}+(l^2-k^2)W=\frac{H}{(\bar{U}-c)^2}, \quad (15)$$

where

$$l^2=\frac{N^2}{(\bar{U}-c)^2}-\frac{d^2\bar{U}/dz^2+2\Gamma d\bar{U}/dz}{\bar{U}-c}-\frac{d\Gamma}{dz}-\Gamma^2. \quad (16)$$

Here l^2 is called the Scorer parameter (Scorer 1949). Boundary conditions for (15) are assumed to be

$$W=0, \quad z=0 \quad (17)$$

$$\frac{dW}{dz}=-iMW, \quad z=z_T, \quad (18)$$

where

$$M=(l^2-k^2)^{1/2} \quad \text{at} \quad z=z_T. \quad (19)$$

Here z_T is the top of the domain. Upper boundary condition (18) is a "radiation condition" that allows energy to propagate upward through the top of the domain (Lindzen 1974) without reflection.

Ground-relative wind $\bar{U}(z)$ in Fig. 21a, $N^2(z)$ in Fig. 21b, and Scorer parameter $l^2(z)$ in Fig. 21c are determined from the horizontally averaged profiles of a 70-km-wide region of the leading portion of the simulated 2D squall line at time $t = 11$ h ($x = -20$ to 50 km in Figs. 9–12). Storm-relative wind can be obtained by subtracting the storm propagation speed (12 m s^{-1}) from the ground-relative wind. Ground-relative phase speed $c = -20$ m s^{-1} (storm-relative phase speed is -32 m s^{-1}) is determined from a time-lapse display of

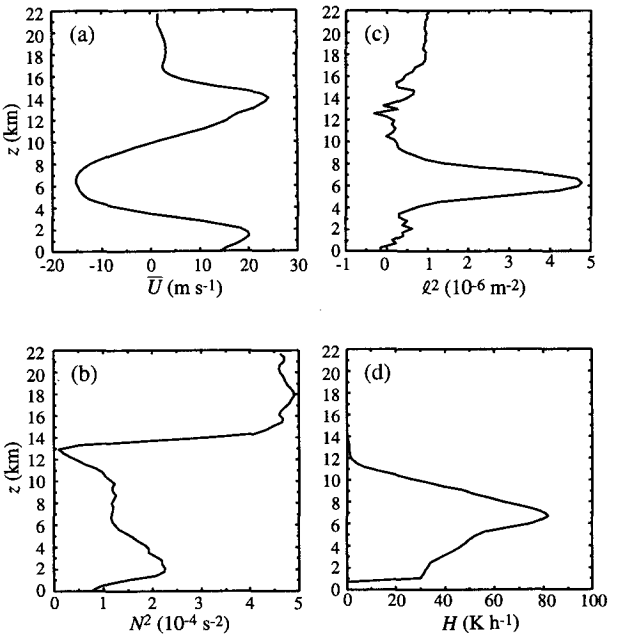

FIG. 21. (a) Vertical profiles of ground-relative wind $\bar{U}(z)$, (b) $N^2(z)$, (c) Scorer parameter $l^2(z)$ averaged horizontally over a 70-km-wide region ($x = -20$ to 50 km), and (d) the smoothed latent heating $H(z)$ for the region $x = 10$ to 26 km for the simulated 2D storm at $t = 11$ h.

model results with a data resolution of 2 min. Local horizontal wavenumber k is determined from the cell separation distance. For the region of $x = 10$–26 km in Figs. 9–12, k is found to be $-2\pi/(16\text{ km})$. A negative wavenumber means FTR-moving waves. The smoothed latent heating profile $H(z)$ (the average heating over one-half a wavelength) in Fig. 21d is determined from numerical model output at $t = 11$ h for that region ($x = 10$–26 km). For given k, c, $\Gamma(z)$, $\bar{U}(z)$, $N^2(z)$, and $H(z)$, we can use the method of Lindzen and Kuo (1969) to solve (15) for $W(z)$ numerically. Note that $W(z)$ is a complex variable because of the radiation condition (18). Therefore, from (14), $\tilde{Q}$ can be expressed in the form

$$\tilde{Q} = H\cos(kx - kct). \tag{20}$$

Then $\tilde{w}$ can be written in the form

$$\tilde{w} = \mathrm{Re}W\cos(kx - kct) - \mathrm{Im}W\sin(kx - kct), \tag{21}$$

where the real part (Re) and the imaginary part (Im) of $W(z)$ are determined from (15), (17), and (18). Hence, $\tilde{u}$ can be determined by substituting (21) into the continuity equation (12),

$$\tilde{u} = \frac{1}{k}\left[\Gamma\,\mathrm{Re}W - \frac{d}{dz}(\mathrm{Re}W)\right]\sin(kx - kct) + \frac{1}{k}\left[\Gamma\,\mathrm{Im}W - \frac{d}{dz}(\mathrm{Im}W)\right]\cos(kx - kct); \tag{22}$$

$\tilde{\pi}$ can be determined by substituting (21) and (22) into the u-momentum equation (7),

$$\tilde{\pi} = -\frac{1}{k}\left[(\bar{U} - c)\left(\Gamma\,\mathrm{Re}W - \frac{d}{dz}\mathrm{Re}W\right) + \frac{d\bar{U}}{dz}\mathrm{Re}W\right]\sin(kx - kct) + \frac{1}{k}\left[(c - \bar{U})\left(\Gamma\,\mathrm{Im}W - \frac{d}{dz}\mathrm{Im}W\right) - \frac{d\bar{U}}{dz}\mathrm{Im}W\right]\cos(kx - kct); \tag{23}$$

and $\tilde{\theta}$ can be determined by substituting (20) and (21) into the thermodynamic equation (9),

$$\tilde{\theta} = \frac{H - N^2\,\mathrm{Re}W}{k(\bar{U} - c)}\sin(kx - kct) + \frac{-N^2\,\mathrm{Im}W}{k(\bar{U} - c)}\cos(kx - kct). \tag{24}$$

6. Discussion

a. Linear theory result

Figure 22a shows the w and p' perturbation fields predicted by the linear theory for the region of $x = 10$–26 km at time $t = 11$ h, and Fig. 22b is the corresponding 2D numerical simulation result. Linear theory predicts the right strength ($\sim$7.9 m s^{-1}) of the updraft at the right level ($\sim$7.3 km) when compared with nonlinear numerical model output (Fig. 22b). Linear theory captures the strong vertical tilt of the phase line in the lower stratosphere (the tilt angle of the phase line from the vertical is 60.6° in Fig. 22a versus 72° in Fig. 22b). Linear theory shows that low pressure perturbations are to the left of the updrafts at low levels (for low pressures p' at $x = 13$–15 km, $z < 7$ km) and to the right of the updrafts at upper levels (for low pressures p' at $x = 21$–23 km, 7 km $< z <$ 14 km), which are also seen in the nonlinear numerical model result. Thus the phase relationship between the p' and w fields is well predicted by linear theory. The amplitude of pressure perturbation p' is somewhat underpredicted at low levels (predicted $p' = -4.3$ mb versus simulated $p' = -5.1$ mb for the low centered at $z = 3$ km, $x = 13$ km) and slightly overpredicted at upper levels (predicted $p' = 1.2$ mb versus simulated $p' = 1.0$ mb for the high centered at $z = 13$ km, $x = 13$ km). However, these discrepancies are minor. The results demonstrate that the multicellular structure is basically controlled by linear gravity wave dynamics.

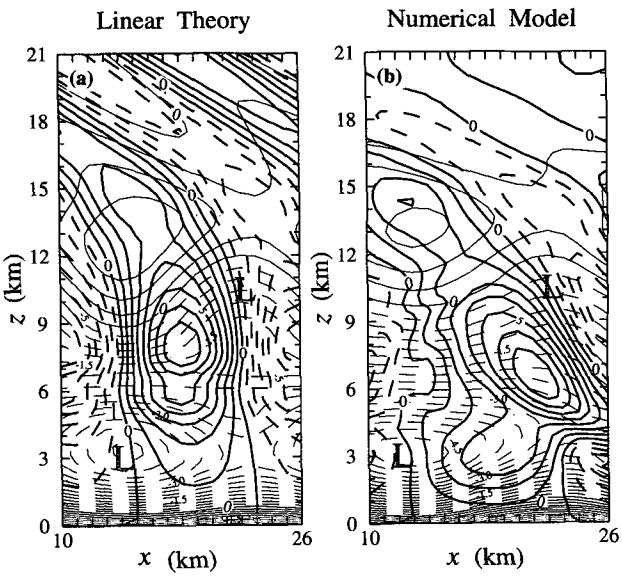

FIG. 22. (a) Vertical velocity (thick line) and pressure perturbation (thin line) fields predicted by linear theory and (b) determined from the 2D simulation for $x = 10$–26 km at $t = 11$ h. Contour interval is 1 m s^{-1} for vertical velocity and 0.3 mb for pressure perturbation; the positive field is in solid lines and the negative field is dashed. A letter L denotes a region of low pressure.

Figure 23a displays the w and u fields predicted by the linear theory for the same region at $t = 11$ h, and Fig. 23b is the corresponding numerical model result. Again, linear theory predicts the phase relationship between the w and u field very well. The amplitude of the u maximum is underpredicted at low levels (predicted

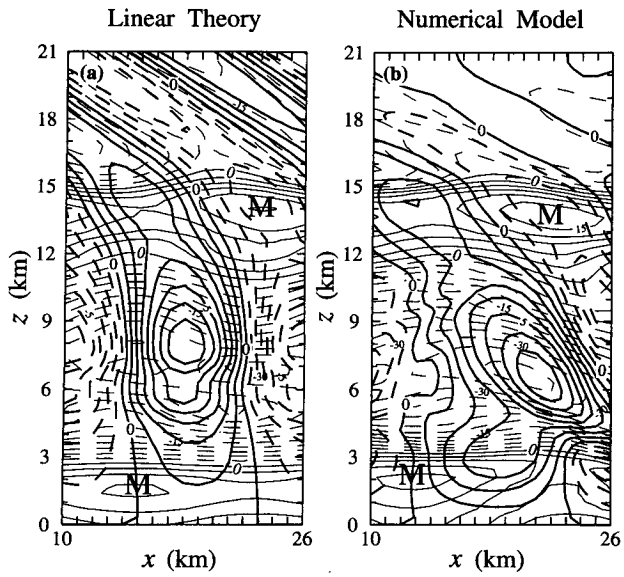

FIG. 23. As in Fig. 22 except for vertical velocity (thick line) and storm-relative horizontal wind (thin line). Contour interval is 1 m s^{-1} for vertical velocity and 3 m s^{-1} for storm-relative horizontal wind. A letter M denotes a region of horizontal wind maximum.

u = 9.5 m s^{-1} versus simulated u = 12.9 m s^{-1} for the maximum centered at z = 1.7 km, x = 13 km) and slightly underpredicted at upper levels (predicted u = 15.2 m s^{-1} versus simulated u = 17.2 m s^{-1} for the maximum centered at z = 14 km, x = 23 km).

In general, the predicted gravity wave perturbations of w, u, and p' by linear theory are in somewhat better agreement with the numerical simulation results in the lower stratosphere (z > 14 km) than in the troposphere (z < 14 km), where nonlinear effects and turbulent mixing are more likely to be important. Nevertheless, the success of linear theory in portraying the cell structure seen in the nonlinear numerical simulation lends confidence to the dynamical explanation of the multicellular structure as a gravity wave phenomenon.

b. *Characteristics of trapped waves in the simulated squall line*

At the leading portion of the simulated squall line, the dominant horizontal wavelengths are λ = 16 to 20 km, and storm-relative phase speeds are c = −20 to −25 m s^{-1}, so the main gravity wave periods in this region are $T = \lambda/c$ = 10.7–16.7 min, which are the same as the generation periods of precipitation cells (11–17 min) at the mature stage (see Fig. 6a). Similar horizontal wavelengths (determined as cell separation distances) were also found by Dudhia et al. (1987) for their 2D simulations of a long-lived west African squall line, although their cellular development periods were much longer. In the trailing stratiform region, the gravity waves become more diffuse with weaker amplitudes, and their wavelengths become longer (λ = 25–35 km) with increasing phase speeds (storm-relative phase speeds are c = −30 to −40 m s^{-1}). The horizontal phase-speed (c_x) formula for 2D internal gravity waves with a constant mean flow $\bar{u}$ is

$$c_x = \bar{u} \pm \frac{N}{(k^2 + m^2)^{1/2}},$$

where m is the vertical wavenumber [Eq. (7.44) of Holton 1992]. The increase of phase speed with increasing horizontal wavelength is a characteristic of the dispersive internal gravity waves. The reason why the wavelengths of gravity waves differ between the convective and stratiform regions is not clear.

The multicellular squall line shows a nice wave train of updraft cells and the significant quadrature relationship between w and p' (u, or θ') fields. The amplitudes of convective cells are well predicted by the linear gravity wave theory. The generation periods of these convective cells are the same as the gravity wave periods. It is clear from these three facts that the convective cells behind the gust front are very likely to be transient gravity wave features.

For a mature squall line, the generation of gravity waves and their associated convective cells by the forced lifting of warm air over the cold pool may be similar to the generation of gravity waves by the forced lifting of air over a mountain. Once buoyancy oscillations are triggered at the leading edge of the cold pool, they are further modulated by the latent heating associated with convective cells. The constant rearward propagation of convective cells within the storm is due to the westward (FTR) phase speeds of their associated gravity waves.

The quadrature relationship (90° phase shift) between w and p' (or u) fields in low levels can also be seen in the simulated Oklahoma squall line on 22 May 1976 by FO (see their Figs. 8 and 10). Fovell and Ogura (1989) further investigated the effects of low-level wind shear on the simulated mature-phase multicell storms. They defined a quasi-equilibrium state as the repetitive multicellular development, and the quasi-equilibrium state was achieved for a very wide range of wind shear intensities. The average period between successive cellular development in their study was relatively constant (17 min), which suggested the existence of a "fundamental oscillation" common to the simulated multicell storms. This relatively constant period of cellular development might be the wave period of the trapped gravity waves in their simulated storms.

c. *Trapping mechanisms*

According to (15), the vertical structure of the gravity waves depends on the relative magnitude of the Scorer parameter l^2 and the horizontal wavenumber. If $l^2 > k^2$, then the wave oscillates in z with vertical wavenumber $(l^2 - k^2)^{1/2}$; that is, it is a vertically propagating wave. If $l^2 < k^2$, then the solution decays with

height (since the solution must be bounded); that is, it is an evanescent or trapped wave.

Trapping of gravity waves in the troposphere is not a result of the strong static stability in the lower stratosphere. This point can be demonstrated in Fig. 24a, which shows the linear theory result when the stratosphere is removed by using a constant tropospheric value of $N = 1.1 \times 10^{-2}\ s^{-1}$ for $z \geq 10$ km. In this case, waves still show the typical trapped-wave phase relationships between w and p' fields in the troposphere (see w and p' fields in Fig. 10). The reason for the waves to be trapped in the mid- to upper levels (6 km $< z <$ 13 km) is the strong decrease of Scorer parameter l^2 with height, analogous to trapped lee waves (Durran 1990). Recalling the definition of the Scorer parameter in (16), it can be seen from Figs. 21a–c that the decrease of Scorer parameter with height in mid- to upper levels (6 km $< z <$ 13 km) results from both an increase of wind speed ($\bar{U} - c$) and a decrease of static stability (N) with height. Curvature of mean flow and other effects indicated in the definition of the Scorer parameter contribute very little to the trapping mechanism in the mid- to upper levels.

Waves are also trapped in low levels ($0 < z < 6$ km). This low-level trapping mechanism is further investigated in Fig. 24b, in which the rigid-lid ground is replaced by an open radiation condition at the lower boundary condition using the same Scorer parameter profile in Fig. 21c. Instead of being trapped, waves in low levels in Fig. 24b show a downward-propagating structure. Note that in the low level ($z < 4.5$ km), waves show an opposite phase relationship between w and p' fields (constant phase line tilts rearward with decreasing height; w is out of phase with p') compared to waves in the lower stratosphere (constant phase line tilts rearward with increasing height; w is in phase with p'). This opposite phase relationship with the upward-propagating waves in the stratosphere ($z > 14$ km) indicates that waves in the lower levels ($z < 4.5$ km) for the open lower-boundary case propagate downward. Therefore, the downward-propagating waves destructively interfere with upward-propagating waves reflected from the ground so that there is no vertical tilt of the phase line. Thus, waves are trapped in low levels ($0 < z < 6$ km) because of the rigid ground.

The trapping mechanism determined from the vertical profile of the Scorer parameter also applies to the internal gravity waves within the oceanic thermocline (Lighthill 1978). The role of the Scorer parameter $l^2(z)$ in determining the waves' vertical structure for the atmospheric internal gravity waves is similar to that of $N^2(z)$ for the oceanic internal gravity waves. Lighthill (1978) indicated that oceanic internal gravity waves might be trapped within the thermocline region when $N^2(z)$ had a substantial vertical gradient (see his Figure 74), which was similar to the vertical profile of the Scorer parameter in Fig. 21c.

Since the vertical variation of $N^2(z)$ in the troposphere ($z < 14$ km) is not as strong as that of $\bar{U}(z)$

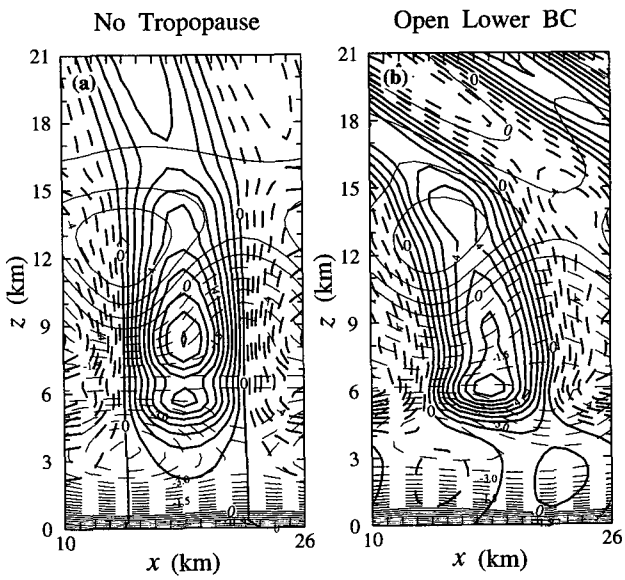

FIG. 24. Vertical velocity (thick line) and pressure perturbation (thin line) fields predicted by linear theory for (a) the no-tropopause case and (b) the open lower-boundary case for x = 10–26 km at t = 11 h. Contour interval is 0.8 m s^{-1} for vertical velocity and 0.3 mb for pressure perturbation; the positive field is in solid lines and the negative field is dashed.

(see Figs. 21a,b), the Scorer parameter is strongly dependent on $\bar{U}(z)$. The strong peak of the Scorer parameter is due to the reverse vertical shear of $\bar{U}(z)$, as a result of RTF flows in upper and lower levels and FTR flows at midlevels. Initially, trapped gravity waves only occur in a narrow area near the convective region. The reverse wind shear associated with RTF and FTR jets is more evident as the storm becomes well developed and mature, and the vertical peak of the Scorer parameter is also more pronounced with a wider trapped gravity wave area. *The evolution of the Scorer parameter is thus a feedback interaction between gravity waves and the storm in which they are embedded.* The integral effect of the convective cells (by their associated pressure perturbations) determines the mean wind profile in the cells' surrounding environment, while the Scorer parameter implied by the mean wind profile determines the vertical characteristics of the convective cells' gravity waves—vertically propagating or trapped.

d. Other trapped waves associated with convection

Kuettner et al. (1987) found internal gravity waves in the free troposphere above a convectively active planetary boundary layer. These waves, commonly referred to as "convection waves," usually occur in a synoptic condition that favors active convection in the boundary layer and considerable vertical wind shear ($>3 \times 10^{-3}\ s^{-1}$) through the lower to middle troposphere. These convection waves are excited when the shallow convection in the presence of shear penetrates into the stable layer above the convective boundary

layer. To some extent, the mechanism is similar to the orographic forcing of gravity waves. From the analysis of aircraft data, Kuettner et al. (1987) found that the convection waves had wavelengths of 5–15 km, vertical wind amplitudes of ± 1–3 m s^{-1}, and a vertical extension of at least 9 km.

Gage et al. (1989) documented the observation of convection waves measured by a VHF wind profiling Doppler radar on 29 June 1985 during the PRE-STORM project. These convection waves were formed as a result of strong surface heating and considerable vertical wind shear above the boundary layer. An analysis of the wave event indicated that these convection waves were trapped in the troposphere owing to the influence of background wind shear.

Hauf (1993) reported aircraft observations of convection waves over southern Germany. The convection waves were forced by shallow moist convection penetrating into an overlaying shear layer centered around the boundary layer top and were trapped in midtropospheric levels by a layer of reduced stability aloft. The same trapped-wave phase relationships between w, p', and θ' as those shown in Figs. 9–12 are displayed in his Fig. 7. The measurements showed that convection waves represented a typical fluid-dynamical mode of a daytime troposphere, and they existed in a vertically propagating mode and a trapped mode.

The "convection waves" of Kuettner et al. (1987), Gage et al. (1989), and Hauf (1993) are forced by shallow convection penetrating into an overlying shear layer. The gravity waves in this study are of larger amplitudes ($\Delta w = \pm 2$–10 m s^{-1}) and have longer wavelengths ($\lambda = 16$–20 km). However, the trapping mechanisms for these gravity waves are similar; that is, they are both trapped in the midtroposphere because of strong vertical wind shear and reduced stability aloft.

7. Conclusions

Traditionally, a multicell storm has been thought of as a cluster of short-lived single cells in which the cold-air outflows from each cell combine to form a large gust front; the convergence along its leading edge is generally strongest in the direction of storm motion. This convergence is envisaged to trigger new cell development along the gust front. The old cell dissipates when a new cell appears ahead of it along the gust front and "cuts off" the old cell's supply of moisture and buoyant air. Each individual cell within a multicell storm is assumed to go through such a life cycle and move roughly with the mean wind. What is meant by "triggering" and "cutting off" has remained unclear.

Two-dimensional and three-dimensional simulations of a midlatitude squall line in this study, using a high-resolution nonhydrostatic convection-resolving model, suggest that the multicellular structure with a squall line can be interpreted physically in terms of gravity waves generated by convection. Time-lapse display of model output demonstrates that *the conventional interpretation of the cutoff process is actually a gravity wave phenomenon.* Once the precipitation-induced cold pool is strong enough, there is a low-level updraft continuously generated at the leading edge of cold pool that propagates at the speed of a density current. *Updraft cells behind this low-level leading edge updraft are transient gravity wave features;* they form by periodically breaking away from the top of the low-level gust-front updraft and propagate rearward at phase speeds of their associated gravity waves, not at the mean airflow speeds as implied by the classic multicell model. The persistence of the gust-front updraft fits the "weak evolution" mode of the multicell model of Foote and Frank (1983). The domination of front-to-rear propagation of gravity waves (as opposed to rear-to-front propagation) is due to the persistent upshear tilt of convective cells at the mature stage when the cold pool intensifies and baroclinic vorticity generation at the leading edge of the cold pool dominates over the ambient horizontal vorticity in the low-level wind shear (Rotunno et al. 1988; Fovell et al. 1992).

A schematic model of the gravity wave structure for a multicellular squall line is presented in Fig. 25 based on the 2D simulation results at $t = 11$ h of the 10–11 June 1985 PRE-STORM squall line. Convective cells in the troposphere exhibit a quadrature relationship between the w and p' (or u) fields that indicates they are vertically trapped gravity waves. This phase relationship between the w and u fields in low levels is confirmed by the wind fields derived from the Doppler radar observations. The gravity waves excited by the continuous low-level lifting at the gust front are trapped in the mid- to upper troposphere because of a strong decrease of Scorer parameter with height as a result of strong vertical wind shear and the decreased static stability aloft. A similar trapping mechanism was indicated by Gage et al. (1989) and Hauf (1993) for shallow trapped convection waves. Waves are also trapped in low levels because of the rigid flat ground. Trapped gravity waves only occur in a narrow area near the convective region initially; as the storm becomes well developed with stronger FTR and RTF jets, producing a stronger decrease of Scorer parameter with height, the trapped-wave area is wider.

Although most of the gravity waves associated with convective cells are trapped in the troposphere, some strong waves can "leak" through the troposphere and reach the stratosphere. Once waves pass into the highly stratified stratosphere, they have the typical structure of vertically propagating gravity waves—w is in phase with p', out of phase with u', and 90° ahead of θ' in the rearward mode, whereas w is in phase with both p' and u' and 90° behind θ' in the forward mode. The gravity waves in the lower stratosphere are mechanically forced by strong convective cells constantly impinging upon the tropopause in the convective region, as explained by Fovell et al. (1992).

Linear theory explains the multicellular structure determined from the nonlinear numerical simulation. Lin-

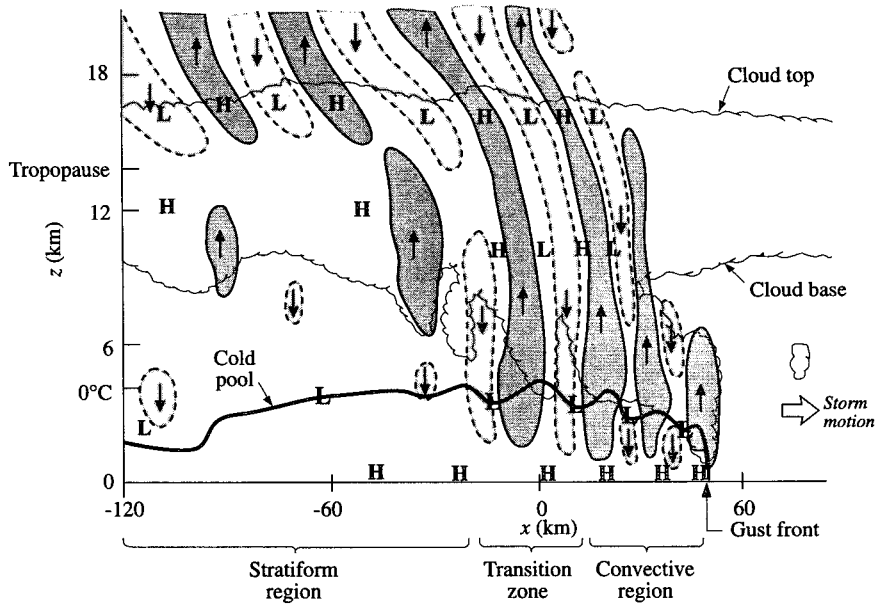

FIG. 25. Schematic model of the gravity wave structure for a mature-stage multicellular squall line based on 2D simulation results at $t = 11$ h. Updrafts greater than 1 m s^{-1} are heavily shaded, and downdrafts less than -1 m s^{-1} are lightly shaded. Heavy line is the cold pool outline defined by the $\theta' = -1$ K contour; cloud shield is defined by the 0.5 g kg^{-1} contour of nonprecipitating hydrometeor mixing ratio ($q_c + q_i = 0.5$ g kg^{-1}; q_c is the cloud water mixing ratio and q_i is the cloud ice mixing ratio). A letter L or H denotes a region of low or high pressure.

ear theory well predicts the amplitudes of w, p', and u' perturbations, the phase relationships between these variables, and the strong vertical tilt of the constant phase line in the lower stratosphere. Linear theory thus gives a dynamical explanation of multicellular thunderstorm structure as a gravity wave phenomenon.

The basic characteristics of these trapped tropospheric gravity waves are wavelengths λ of 16–20 km, storm-relative phase speeds c of -20 to -25 m s^{-1}, and periods ($T = \lambda/c$) of 10.7–16.7 min, which are consistent with the generation periods of precipitation cells at the mature stage in the leading portion of the storm. In the trailing stratiform region, the amplitudes of these gravity waves become weaker, but their wavelengths become longer ($\lambda = 25$–35 km) with faster phase speeds (storm-relative phase speeds are $c = -30$ to -40 m s^{-1}), in accordance with the dispersion relationship for internal gravity waves.

This gravity wave explanation for the multicellular structure of thunderstorms and squall lines may lead to a new understanding of convective momentum transport. The different characteristics (wavelengths, phase speeds) of the gravity waves between the convective and stratiform region may explain why convective momentum transport has different characteristics in the convective and stratiform regions of a squall line with a trailing stratiform region (Gallus and Johnson 1992; Yang and Houze 1992). The gravity wave interpretation also might be useful for the parameterization of multicell-type convective systems in large-scale models.

Acknowledgments. Professor R. G. Fovell guided the early modeling of the storm. Professor M. I. Biggerstaff provided the dual-Doppler radar analysis. Comments by Professor J. R. Holton, Professor D. R. Durran, Dr. David Kingsmill, Dr. Joan Alexander, and reviewers are appreciated. Candace Gudmundson edited the manuscript and Kay Dewar drafted some of the figures. The simulation was performed at the National Center for Supercomputing Applications at the University of Illinois at Urbana–Champaign. This research was supported by National Science Foundation Grant ATM-9101653.

APPENDIX

Derivation of the Governing Equation for $\tilde{w}$

In order to simplify the mathematical expression, we use a subscript x as a partial differentiation with respect to x, that is, $\partial/\partial x(\ ) \rightarrow (\ )_x$, and also use this shorthand notation T such that $\partial/\partial T(\ ) = (\partial/\partial t + \bar{U}\partial/\partial x)(\ ) \rightarrow (\ )_T$. Subtracting $(\partial/\partial z + \Gamma)(7)$ from $\partial(8)/\partial x$, we can eliminate $\tilde{\pi}$ between (7) and (8):

$$\tilde{w}_{xT} - \tilde{\theta}_x - \tilde{u}_{zT} - \tilde{w}_z\bar{U}_z - \tilde{w}\bar{U}_{zz} - \Gamma\tilde{u}_T - \Gamma\tilde{w}\bar{U}_z = 0. \quad \text{(A1)}$$

Adding $\partial(9)/\partial x$ to $\partial(\text{A1})/\partial T$, we can eliminate $\tilde{\theta}$:

$$\tilde{w}_{TxT} - \tilde{u}_{TzT} - (\tilde{w}_{Tz} + \Gamma\tilde{w}_T)\bar{U}_z - \tilde{w}_T\bar{U}_{zz} - \Gamma\tilde{u}_{TT} + N^2\tilde{w}_x - \tilde{Q}_x = 0. \quad \text{(A2)}$$

Taking $\partial(\text{A2})/\partial x$, we can eliminate $\tilde{u}$ with the aid of (12) to yield a single equation for $\tilde{w}$:

$$\tilde{w}_{TTxx} + \tilde{w}_{TTzz} - \tilde{w}_{Tx}\bar{U}_{zz} - (\Gamma^2 + \Gamma_z)\tilde{w}_{TT} - 2\Gamma\bar{U}_z\tilde{w}_{Tx} + N^2\tilde{w}_{xx} - \tilde{Q}_{xx} = 0. \quad \text{(A3)}$$

Equation (A3) is the same as (13) after converting shorthand notations to their original mathematical expressions.

REFERENCES

Biggerstaff, M. I., and R. A. Houze, Jr., 1991a: Kinematic and precipitation structure of the 10–11 June 1985 squall line. *Mon. Wea. Rev.*, **119,** 3034–3065.

——, and ——, 1991b: Midlevel vorticity structure of the 10–11 June 1985 squall line. *Mon. Wea. Rev.*, **119,** 3066–3079.

——, and ——, 1993: Kinematics and microphysics of the transition zone of the 10–11 June 1985 squall line. *J. Atmos. Sci.*, **50,** 3091–3110.

Bluestein, H. B., and M. H. Jain, 1985: Formation of mesoscale lines of precipitation: Severe squall lines in Oklahoma during spring. *J. Atmos. Sci.*, **42,** 1711–1732.

Braun, S. A., and R. A. Houze Jr., 1994: The transition zone and secondary maximum of radar reflectivity behind a midlatitude squall line: Results retrieved from Doppler radar data. *J. Atmos. Sci.*, **51,** 2733–2755.

Bretherton, F. P., 1966: The propagation of groups of internal gravity waves in a shear flow. *Quart. J. Roy. Meteor. Soc.*, **92,** 466–480.

Browning, K. A., 1962: Cellular structure of convective storms. *Meteor. Mag.*, **91,** 341–350.

——, 1977: The structure and mechanisms of hailstorms. *Hail: A Review of Hail Science and Hail Suppression,* G. B. Foote and C. A. Knight, Eds., American Meteorological Society, 1–43.

——, J. C. Fankhauser, J.-P. Chalon, P. J. Eccles, R. C. Strauch, F. H. Merrem, D. J. Musil, E. L. May, and W. R. Sand, 1976: Structure of an evolving hailstorm. Part V: Synthesis and implications for hail growth and hail suppression. *Mon. Wea. Rev.*, **104,** 603–610.

Byers, H. R., and R. R. Braham Jr., 1949: *The Thunderstorm.* U.S. Government Printing Office, Washington, D.C., 287 pp.

Chalon, J.-P., J. C. Fankhauser, and P. J. Eccles, 1976: Structure of an evolving hailstorm. Part I: General characteristics and cellular structure. *Mon. Wea. Rev.*, **104,** 564–575.

Cunning, J. B., 1986: The Oklahoma–Kansas Preliminary Regional Experiment for STORM-Central. *Bull. Amer. Meteor. Soc.*, **67,** 1478–1486.

Doty, K. G., and D. J. Perkey, 1993: Sensitivity of trajectory calculations to the temporal frequency of wind data. *Mon. Wea. Rev.*, **121,** 387–401.

Droegemeier, K. K., and R. B. Wilhelmson, 1985: Three-dimensional numerical modeling of convection produced by interacting thunderstorm outflows. Part I: Control simulation and low-level moisture variations. *J. Atmos. Sci.*, **42,** 2381–2403.

Dudhia, J. M., W. M. Moncrieff, and D. W. K. So, 1987: The two-dimensional dynamics of West African squall lines. *Quart. J. Roy. Meteor. Soc.*, **113,** 121–146.

Durran, D. R., 1990: Mountain waves and downslope winds. *Atmospheric Processes over Complex Terrain,* W. Blumen, Ed., American Meteorological Society, 59–81.

Foote, G. B., and H. W. Frank, 1983: Case study of a hailstorm in Colorado. Part III: Airflow from triple-Doppler measurements. *J. Atmos. Sci.*, **40,** 686–707.

Fovell, R. G., and Y. Ogura, 1988: Numerical simulation of a midlatitude squall line in two dimensions. *J. Atmos. Sci.*, **45,** 3846–3879.

——, and ——, 1989: Effects of vertical wind shears on numerically simulated multicell storm structure. *J. Atmos. Sci.*, **46,** 3144–3176.

——, D. Durran, and J. R. Holton, 1992: Numerical simulations of convectively generated stratospheric gravity waves. *J. Atmos. Sci.*, **49,** 1427–1442.

Gage, K. S., W. L. Ecklund, and D. A. Carter, 1989: Convection waves observed using a VHF wind-profiling Doppler radar during the PRE-STORM experiment. *Proc. 24th Conf. on Radar Meteor.,* Tallahassee, FL, Amer. Meteor. Soc., 705–708.

Gallus, W. A., Jr., and R. H. Johnson, 1992: The momentum budget of an intense midlatitude squall line. *J. Atmos. Sci.*, **49,** 422–450.

Gill, A. E., 1982: *Atmosphere–Ocean Dynamics.* Academic Press, 662 pp.

Hauf, T., 1993: Aircraft observation of convection waves over southern Germany—A case study. *Mon. Wea. Rev.*, **121,** 3282–3290.

Holton, J. R., 1992: *An Introduction to Dynamic Meteorology.* 3d ed. Academic Press, 507 pp.

Johnson, R. H., and P. J. Hamilton, 1988: The relationship of surface pressure features to the precipitation and airflow structure of an intense midlatitude squall line. *Mon. Wea. Rev.*, **116,** 1444–1472.

Klemp, J. B., and R. B. Wilhelmson, 1978: The simulation of three-dimensional convective storm dynamics. *J. Atmos. Sci.*, **35,** 1070–1096.

Kuettner, J. P., P. A. Hildebrand, and T. L. Clark, 1987: Convection waves: Observations of gravity wave systems over convectively active boundary layers. *Quart. J. Roy. Meteor. Soc.*, **113,** 445–467.

Lighthill, J., 1978: *Waves in Fluids.* Cambridge University Press, 504 pp.

Lin, Y. L., R. D. Farley, and H. D. Orville, 1983: Bulk parameterization of the snow field in a cloud model. *J. Climate Appl. Meteor.*, **22,** 1066–1092.

Lindzen, R. S., 1974: Wave-CISK in the tropics. *J. Atmos. Sci.*, **31,** 156–179.

——, and H.-L. Kuo, 1969: A reliable method for the numerical integration of a large class of ordinary and partial differential equations. *Mon. Wea. Rev.*, **97,** 732–734.

Marwitz, J. D., 1972: The structure and motion of severe hailstorms. Part II: Multicell storms. *J. Appl. Meteor.*, **11,** 180–188.

Moncrieff, M. W., and M. J. Miller, 1976: The dynamics and simulation of tropical cumulonimbus and squall lines. *Quart. J. Roy. Meteor. Soc.*, **102,** 373–394.

Newton, C. W., and J. C. Fankhauser, 1975: Movement and propagation of multicellular convective storms. *Pure Appl. Geophys.*, **113,** 747–764.

Nicholls, M. E., and M. J. Weissbluth, 1988: A comparison of two-dimensional and quasi-three-dimensional simulations of a tropical squall line. *Mon. Wea. Rev.*, **16,** 2437–2452.

Potter, B. E., 1991: Improvement to a commonly used cloud microphysical bulk parameterization. *J. Appl. Meteor.*, **30,** 1040–1042.

Rotunno, R., J. B. Klemp, and M. L. Weisman, 1988: A theory for strong, long-lived squall lines. *J. Atmos. Sci.*, **45,** 463–485.

Rutledge, S. A., R. A. Houze Jr., M. I. Biggerstaff, and T. Matejka, 1988: The Oklahoma–Kansas mesoscale convective system of 10–11 June 1985: Precipitation structure and single-Doppler radar analysis. *Mon. Wea. Rev.*, **116,** 1409–1430.

Sanders, F., and K. A. Emanuel, 1977: The momentum budget and temperature evolution of a mesoscale convective system. *J. Atmos. Sci.*, **34,** 322–330.

Sawyer, J. S., 1960: Numerical calculation of the displacements of a stratified airstream crossing a ridge of small height. *Quart. J. Roy. Meteor. Soc.*, **86,** 326–345.

Scorer, R. S., 1949: Theory of waves in the lee of mountains. *Quart. J. Roy. Meteor. Soc.*, **75,** 41–56.

Smull, B. F., and R. A. Houze, 1987: Rear inflow in squall lines with trailing stratiform precipitation. *Mon. Wea. Rev.*, **115,** 2869–2889.

Weisman, M. L., and J. B. Klemp, 1982: The dependence of numerically simulated convective storms on wind shear and buoyancy. *Mon. Wea. Rev.*, **110,** 504–520.

——, and ——, 1984: The structure and classification of numerically simulated convective storms in directionally varying wind shears. *Mon. Wea. Rev.*, **112,** 2479–2498.

——, and ——, 1986: Characteristics of convective storms. *Mesoscale Meteorology and Forecasting,* P. S. Ray, Ed., American Meteorological Society, 331–358.

Wilhelmson, R. B., and Y. Ogura, 1972: The pressure perturbation and the numerical modeling of a cloud. *J. Atmos. Sci.*, **29,** 1295–1307.

——, and C.-S. Chen, 1982: A simulation of the development of successive cells along a cold outflow boundary. *J. Atmos. Sci.*, **39,** 1466–1483.

Yang, M.-J., and R. A. Houze Jr., 1992: A numerical study of the momentum budget of a squall line. Preprints, *11th Int. Conf. on Clouds and Precipitation,* Montreal, Canada, American Meteorological Society, 719–722.

Zhang, D.-L., and K. Gao, 1989: Numerical simulation of an intense squall line during the 10–11 June 1985 PRE-STORM. Part II. Rear inflow, surface wake lows and stratiform precipitation. *Mon. Wea. Rev.*, **117,** 2067–2094.

——, ——, and D. B. Parsons, 1989: Numerical simulation of an intense squall line during the 10–11 June 1985 PRE-STORM. Part I. Model verification. *Mon. Wea. Rev.*, **117,** 960–994.